Molecular Therapy
Original Article

The phosphatidylserine flippase β-subunit *Tmem30a* is essential for normal insulin maturation and secretion

Yeming Yang,[1,2] Kuanxiang Sun,[2] Wenjing Liu,[2] Xiao Li,[2] Wanli Tian,[2] Ping Shuai,[1,2,4] and Xianjun Zhu[1,2,3,4,5,6]

[1]Health Management Center, Sichuan Provincial People's Hospital, School of Medicine, University of Electronic Science and Technology of China, Chengdu, Sichuan 610072, China; [2]The Sichuan Provincial Key Laboratory for Human Disease Gene Study, Center for Medical Genetics, Prenatal Diagnosis Center, Sichuan Provincial People's Hospital, University of Electronic Science and Technology of China, Chengdu, Sichuan 610072, China; [3]Key Laboratory of Tibetan Medicine Research, Chinese Academy of Sciences and Qinghai Provincial Key Laboratory of Tibetan Medicine Research, Northwest Institute of Plateau Biology, Xining, Qinghai 810008, China; [4]Research Unit for Blindness Prevention of Chinese Academy of Medical Sciences (2019RU026), Sichuan Academy of Medical Sciences and Sichuan Provincial People's Hospital, Chengdu, Sichuan 610072 China; [5]Natural Products Research Center, Institute of Chengdu Biology, Sichuan Translational Medicine Hospital, Chinese Academy of Sciences, Chengdu, Sichuan 610072, China; [6]Department of Ophthalmology, First People's Hospital of Shangqiu, Shangqiu, Hennan 476100, China

The processing, maturation, and secretion of insulin are under precise regulation, and dysregulation causes profound defects in glucose handling, leading to diabetes. Tmem30a is the β subunit of the phosphatidylserine (PS) flippase, which maintains the membrane asymmetric distribution of PS. Tmem30a regulates cell survival and the localization of subcellular structures and is thus critical to the normal function of multiple physiological systems. Here, we show that conditional knockout of Tmem30a specifically in pancreatic islet β cells leads to obesity, hyperglycemia, glucose intolerance, hyperinsulinemia, and insulin resistance in mice, due to insufficient insulin release. Moreover, we reveal that *Tmem30a* plays an essential role in clathrin-mediated vesicle transport between the *trans* Golgi network (TGN) and the plasma membrane (PM), which comprises immature secretory granule (ISG) budding at the TGN. We also find that *Tmem30a* deficiency impairs clathrin-mediated vesicle budding and thus blocks both insulin maturation in ISGs and the transport of glucose-sensing Glut2 to the PM. Collectively, these disruptions compromise both insulin secretion and glucose sensitivity, thus contributing to impairments in glucose-stimulated insulin secretion. Taken together, our data demonstrate an important role of *Tmem30a* in insulin maturation and glucose metabolic homeostasis and suggest the importance of membrane phospholipid distribution in metabolic disorders.

INTRODUCTION

Type 2 diabetes mellitus (T2DM) is a metabolic disorder characterized by both impaired insulin production and peripheral insulin resistance[1–3] and is increasing in prevalence in many regions. β cells in the pancreas islets regulate synthesis and secretion of insulin in response to elevated blood glucose concentration, initially in the form of preproinsulin, which is encoded by *Ins* genes (in mice, by *Ins1* and *Ins2*). Newly synthesized preproinsulin is localized to the endoplasmic reticulum (ER) membrane and, after translocation across the ER membrane, is processed to proinsulin. Proinsulin then undergoes oxidative folding and is transported from the ER to the Golgi complex. Properly folded proinsulin is then packaged and sorted in the *trans* Golgi network (TGN) into immature secretory granules (ISGs).[4] After budding from the TGN, ISGs undergo multiple maturation steps to form mature secretory granules. During this maturation process, the cleavage of proinsulin results in the formation of c-peptide and mature insulin. The mature-insulin-containing dense core vesicles (DCVs) then accumulate at a cytoplasmic reserve pool.[5] Upon stimulation with high glucose, a series of events were activated, including glucose uptake by Glut2 initially in β cells, elevation of the ATP/ADP ratio by mitochondrial metabolism, closure of ATP-sensitive K^+ channels, and Ca^{2+} influx through voltage-gated Ca^{2+} channels following plasma membrane (PM) depolarization, which triggers the Ca^{2+}-dependent exocytosis of insulin granules.[6] Rapid insulin release promotes glucose uptake by peripheral tissues to maintain glucose homeostasis.

The asymmetric distribution of phospholipids across cellular membranes is essential for many cellular processes, including vesicle trafficking that regulates insulin processing and secretion.[7,8] Phospholipid asymmetry in the PM and intracellular membranes is established by phospholipid flippases, which belong to the P4-ATPase family, using energy from ATP hydrolysis. Flippase-mediated membrane phospholipid asymmetry is critical to vesicle-mediated protein transport in the Golgi complex and endosomal systems.[9,10] As such, when flippases malfunction, cellular secretion may in turn be affected.

Received 22 October 2020; accepted 19 April 2021;
https://doi.org/10.1016/j.ymthe.2021.04.026.

Correspondence: Xianjun Zhu, Sichuan Provincial People's Hospital, University of Electronic Science and Technology of China, Chengdu, Sichuan 610072, China.
E-mail: xjzhu@uestc.edu.cn
Correspondence: Ping Shuai, Sichuan Provincial People's Hospital, University of Electronic Science and Technology of China, Chengdu, Sichuan 610072, China.
E-mail: shuaiping@med.uestc.edu.cn

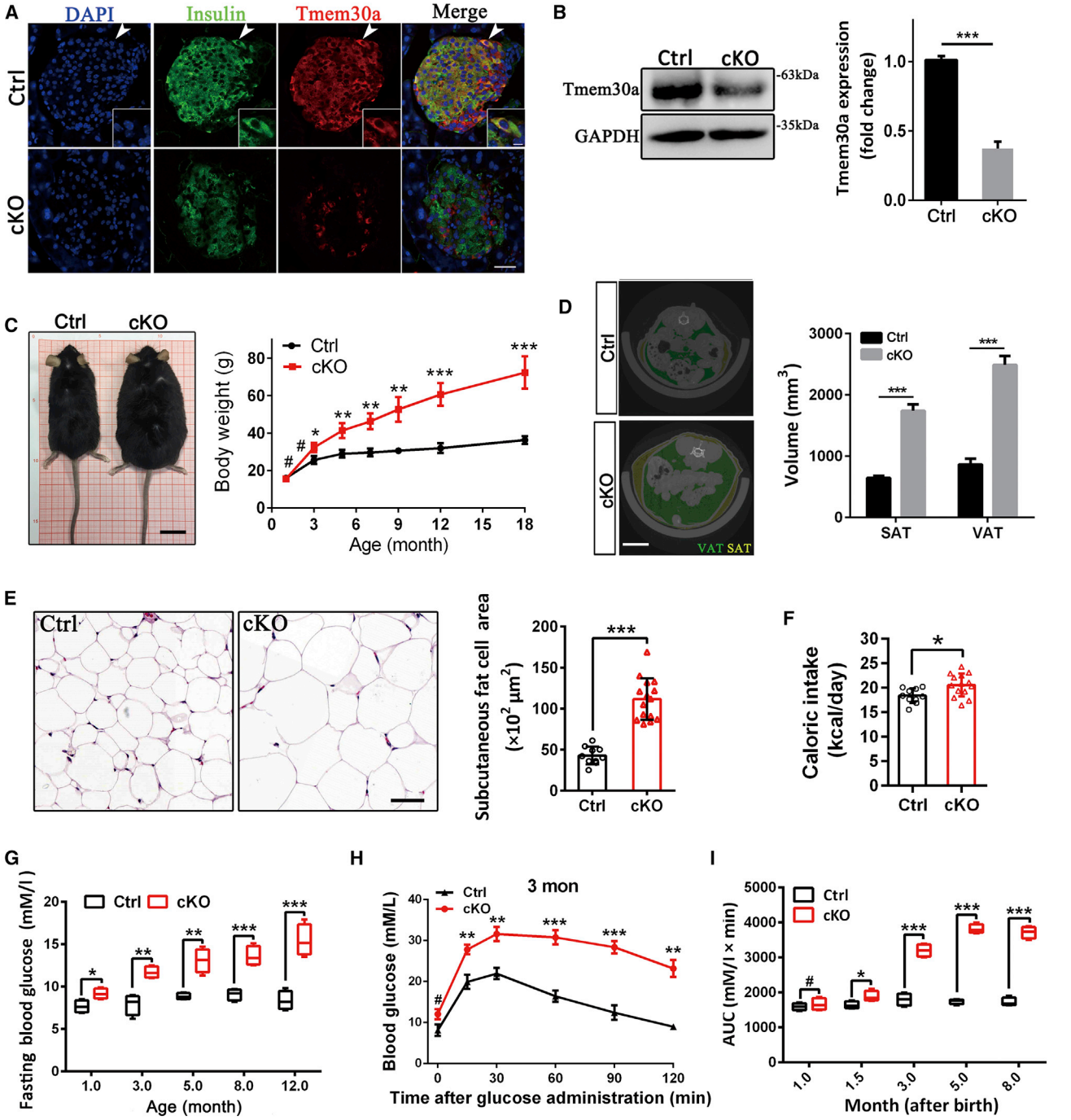

Figure 1. *Tmem30a* cKO mice are obese and glucose intolerant

(A) Immunofluorescence labeling of pancreatic cryosections from *Tmem30a*$^{loxP/loxP}$ (Ctrl) and *Tmem30a*$^{loxP/loxP}$; *Ins2-Cre* (cKO) mice at P30 for TMEM30A (red), insulin (β cells, green), and DAPI (blue). Scale bar: 50 μm. (B) Expression of TMEM30A protein in the pancreatic islets of cKO mice, as shown by western blot (left) of total lysates of the isolated islets from control and cKO mice and by statistical data (right) (n = 12 from 3 mice). (C) Gross appearance of control and cKO mice (left image) and quantification of the body weight of each genotype over time (chart at right; n = 6). Scale bar: 2 cm. (D) Micro-CT scanning images of visceral (VAT, green) and subcutaneous (SAT, yellow) fat (8 mm above the top of the iliac bone) in 12-month-old control and cKO mice (n = 5). (E) H&E staining of SAT of 5-month-old control and cKO mice (n = 9 for control and n = 15 for cKO). Scale bar: 50 μm. (F) Energy intake of control and cKO mice. Mice were singly housed and food intake was measured. The food intake was conducted at 3 months

(legend continued on next page)

Most P4-ATPases require a noncatalytic β subunit to form a functional phospholipid flippase complex in the membrane.[11–15] Transmembrane protein 30 (TMEM30) (also known as CDC50) binds to the P4-ATPases to form a heterodimer, and mammals express three members of the TMEM30 family—namely, TMEM30A, TMEM30B, and TMEM30C—all of which are N-glycosylated proteins with two transmembrane segments.[15] Tmem30a is the most abundantly expressed Tmem30 protein and interacts with 11 of 14 P4-ATPases, thus exerting essential roles in maintaining flippase activity across a multitude of tissues, including neural tissue, the retina, liver, and hematopoietic cells.[11,13–16] Moreover, emerging studies using mouse models have indicated that *Tmem30a* deficiency leads to multiple disease phenotypes in various tissues, including retina, liver, and cerebellum.[17–22] These studies highlight the fundamental roles of *Tmem30a* in maintaining the normal physiology of various tissues, which function via vesicle-mediated protein transport. However, the role of *Tmem30a* in the endocrine system, another system with high secretory activity, remains elusive.

To date, several P4-ATPases have been associated with diabetes-related disease. Specifically, mutations in the P4-ATPase *Atp10a* lead to glucose intolerance, insulin resistance, obesity, and fatty liver disease, due to a resulting defect in Glut4 vesicle biogenesis and membrane-directed trafficking.[23–25] Similarly, *Atp10d* has been implicated in obesity and high-fat-diet-induced insulin resistance in mice.[26] Moreover, a previous study found that ATP8B1, ATP8B2, and ATP9A, as well as TMEM30A, are abundantly expressed in human and rat pancreatic β cells.[27] In humans, the genomic region encompassing *ATP10A* was identified as a risk locus in a genome-wide association study (GWAS) of insulin resistance in an African American cohort.[28] Moreover, the CpG methylation state of *ATP10A* has been associated with diet-induced weight loss.[29] However, Tmem30a has not been reported to be clinically relevant in any diabetic models or in human diabetes, and its roles in diabetes-related disease remain elusive. Given the essential roles of the flippase complex in vesicle-mediated protein transport, TMEM30A likely plays essential roles in secretion activity of pancreatic β cells, and its *in vivo* function in β cells warrants further investigation.

To investigate the role of *Tmem30a* in pancreatic β cells, we set out to generate a β cell-specific knockout mouse model of *Tmem30a*. Here, we demonstrate that conditional knockout (cKO) of *Tmem30a* in mouse pancreatic β cells leads to diabetes-like symptoms characterized by impaired insulin secretion, glucose intolerance, insulin resistance, and obesity. This phenotype is most likely due to both impaired budding of insulin secretory granules from the TGN and reduced transport of glucose transporter 2 (Glut2) to the membrane in β cells, suggesting critical roles of Tmem30a in maintaining insulin secretion as well as glucose sensing. Mechanistically, we find that TMEM30A is essential for clathrin-mediated vesicle transport between the TGN and PM, as it regulates the activity of phospholipid flippases, which mediate the rapid phospholipid flipping required for membrane curvature during vesicle secretion. Collectively, our studies using both a genetics knockout mouse model and pancreatic β cell lines demonstrate that *Tmem30a* is a crucial regulator of insulin secretion in pancreatic β cells. In addition, our results demonstrate the importance of the phospholipid composition of the membrane for normal β cell function, blood glucose control, and metabolic homeostasis.

RESULTS

Generation of a pancreatic β cell-specific knockout model of *Tmem30a*

The β subunit of the flippase complex TMEM30A plays essential roles in protein trafficking and is likely important for secretory activity in pancreatic β cells. To corroborate a previous study in which *Tmem30a* expression was shown in human and rat pancreatic islets,[27] we began by examining the expression of *Tmem30a* in mouse pancreatic islets. Frozen sections of mouse pancreas were double-immunostained with a specific antibody against TMEM30A[17–19,21,22] and an insulin antibody to mark β cells. Confocal imaging confirmed that TMEM30A is expressed in pancreatic islets, including in insulin-marked β cells (Figure 1A), implying an association between Tmem30a expression and insulin synthesis and/or secretion.

To investigate the potential functional roles of *Tmem30a* in pancreatic β cells, we first generated mice with β cell-specific *Tmem30a* ablation by first crossing *Tmem30a* exon 3 floxed mice ($Tmem30a^{loxP/loxP}$) with Ins2-Cre mice, in which *Cre* is targeted to the *Ins2* locus, and thus Cre expression is under the control of the endogenous β cell Ins2 promoter.[30] Their progeny were next intercrossed to yield littermates $Tmem30a^{loxP/loxP}$; *Ins2-Cre* (*Tmem30a* cKO) and $Tmem30a^{loxP/loxP}$ (used as control) (Figure S1A). In addition, the reporter line ROSA26-tdTomato was used to monitor Ins2-Cre expression in β cells. To this end, cKO mice were mated with ROSA26-tdTomato reporter mice to generate $Tmem30a^{loxP/loxP}$; *Ins2-Cre; ROSA* mice, in which the Cre enzyme removes the STOP element and results in the expression of tdTomato (red fluorescence) in β cells (Figure S1B).

The pancreases of $Tmem30a^{loxP/loxP}$; *Ins2-Cre; ROSA* mice were harvested, and we next labeled the tdTomato-expressing cells using insulin and glucagon antibodies to mark β cells and α cells, respectively. tdTomato-expression was restricted to insulin-positive β cells and absent in glucagon-labeled α cells, indicating the specificity of Ins2-Cre expression (Figure S1C). We confirmed this result by coimmunostaining pancreatic sections from *Tmem30a* cKO and control mice with antibodies for TMEM30A and insulin. Although still expressed in other islet cells, TMEM30A did not extensively co-stain with insulin, implying the specific deletion of *Tmem30a* in β cells of *Tmem30a*

old and expressed in kcal per day per mouse (n = 9 for control mice and n = 10 for cKO mice). (G) Fasting blood glucose levels of control and cKO mice with age (n = 6). (H) Evaluation of glucose tolerance by IPGTT in 3-month-old control and cKO mice (n = 6). (I) Blood glucose (area under the curve, AUC) calculated from IPGTT data obtained from control and cKO mice over time (n = 8). $Tmem30a^{loxP/loxP}$ mice were used as controls in all panels. Student's t test was used for (B), (C), (E), (F), and (G)–(I), and Mann-Whitney U test was used for (D). *p < 0.05; **p < 0.01; ***p < 0.001. #, not significant. Data are presented as the means ± SEM.

cKO mice (Figure 1A). Western blotting analysis of isolated pancreas islets further verified the depletion efficiency. The TMEM30A protein level in the *Tmem30a* cKO islets was reduced to 37% of that of control littermates (Figure 1B). Considering that β cells constitute 70% of the cellular composition of pancreatic islets in mice,[31] and that *Tmem30a* expression is not restricted to β cells, the efficiency of deletion of *Tmem30a* from β cells was fairly robust.

Tmem30a cKO mice fed on regular chow diet exhibited obesity and developed hepatic injury

Tmem30a cKO mice were born at Mendelian ratios. As metabolism is influenced by sex hormones in female mice, phenotypic analysis was first performed using the male littermates. Adult *Tmem30a* cKO mice were fertile, and no difference from controls ($Tmem30a^{loxP/loxP}$) was observed in their birth rate. However, 3 months after birth, *Tmem30a* cKO mice exhibited rapid increases in body weight on a normal chow diet that surpassed those of control mice ($Tmem30a^{loxP/loxP}$) (Figure 1C). Computed tomographic (CT) analysis of aged mice revealed that the volumes of both subcutaneous and visceral fat depots were significantly increased in cKO mice compared to controls (Figure 1D). Moreover, hematoxylin and eosin (H&E) staining of white adipose tissue (WAT) sections from obese cKO mice showed increased adipocyte size relative to controls ($Tmem30a^{loxP/loxP}$) (Figure 1E). Additionally, no obvious difference in daily caloric intake was observed for 2-month-old control (18.39 ± 0.48 kcal/day) and cKO mice (21.59 ± 0.62 kcal/day) (Figure 1F). To reveal the underlying mechanisms of weight gain of cKO mice, 5-month-old control and cKO mice on normal chow were subjected to a multi-day metabolic cage study. Whole-body rates of both oxygen consumption (VO_2) and carbon dioxide production (VCO_2) were declined in cKO mice compared to control at day period, indicating a decreased rate of metabolism (Figures S2A and S2B). However, there was no difference in the respiratory exchange ratio (RER) or heat production (Figure S2C), demonstrating similar substrate preferences and normal circadian shifts between glucose and fatty acid oxidation. Importantly, the cKO mice showed less total distance traveled (DIST) during the test period compared to control mice (Figure S2D), indicating decreased physical activity. These results suggest that the elevated body weight of the cKO mice should be due to a change in decreased rate of metabolism and physical activity.

Since obesity usually induces liver injury in human and animal models,[32–34] we next examined the liver of aged *Tmem30a* cKO mice. Surprisingly, the 8-month-old cKO mice had presented severe hepatic steatosis, detected morphologically and microscopically (Figure S3A). H&E staining showed obvious lipid accumulation in the hepatocytes of cKO mice (Figure S3A, arrows). At 18 months of age, 27.6% of *Tmem30a* cKO mice developed hepatic cirrhosis (Figures S3B and S3D). Masson staining confirmed liver injury and elevated collagen deposition, indicating hepatic fibrosis in *Tmem30a* cKO mice compared with control ($Tmem30a^{loxP/loxP}$) (Figure S3B). Ultimately, hepatic cirrhosis progressed to hepatocellular carcinoma (HCC) in ~17.8% of cKO mice at 22 months of age (Figures S3C and S3D). These results indicated the obesity-induced hepatic pathological changes in *Tmem30a* cKO mice. Importantly, the cKO mice spontaneously developed these liver lesions even on a normal diet, which should derive from disordered glucose/lipid metabolism.

To further investigate the expression level changes of *Tmem30a* in other tissues (especially in liver, WAT, and muscle) of cKO mice, total RNA of multiple tissues from control and cKO mice was extracted and subjected to quantitative PCR (qPCR) analysis, which indicated that the expression level of *Tmem30a* in other tissues was unchanged when Tmem30a was deleted in β cells (Figure S4).

Glucose intolerance, islet hyperplasia, and insulin resistance in cKO mice

We next examined the effect of β cell-specific *Tmem30a* deficiency on glycemic control. We observed steady increase in fasting blood glucose with age in cKO mice, whereas glucose levels in control mice were stable over time (Figure 1G). During the intraperitoneal glucose tolerance test (IPGTT), 3-month-old cKO mice exhibited significant glucose intolerance, which worsened with age (Figures 1H and 1I). H&E staining of pancreatic sections from 8-month-old mice manifested that the cKO mice had dramatically larger islets than control mice (Figures S5A and S5B), which has occurred at a young age (Figures S5C and S6). Indeed, using H&E staining, islet hyperplasia was first detected at 6 weeks of age, accompanied by hyperglycemia and impaired glucose-stimulated insulin secretion (GSIS) response (Figures S7A–S7E).

We then performed immunostaining with antibodies against insulin (β cells) and glucagon (α cells) to analyze changes in islet cellular composition in 5- and 10-month-old mice. An increase in β cell mass was observed in *Tmem30a* cKO mice at both time points, as well as a scattered and disorganized distribution of α cells within the cKO islet (Figure S5D). Compared to that of controls, though, the proportion of glucagon-positive α cells in the total number of cells (nuclei) in islets was unaltered (Figure S5F) in cKO mice at both ages. And no significant difference was found in the mRNA or serum levels (after 6 h of fasting) of glucagon between control ($Tmem30a^{loxP/loxP}$) and cKO isolated islets (Figures S8A and S8B). However, the intensity of insulin staining fluorescence was markedly decreased in hyperplastic *Tmem30a* cKO islets, indicating reduced insulin content in these mutant β cells (Figures S5D and S5E).

Next, GSIS assays revealed that both fasting basal levels of serum insulin and glucose-stimulated insulin release were significantly elevated in 8-month-old *Tmem30a* cKO mice relative to control mice ($Tmem30a^{loxP/loxP}$) (Figure S5G), which may result from the excessive proliferation of β cells. Moreover, the intraperitoneal insulin tolerance test (IPITT) suggested that the insulin sensitivity of cKO mice was impaired relative to controls, as they showed higher blood glucose concentrations at 15 min after insulin injection and prolonged hyperglycemia over time (Figure S5H), suggesting insulin resistance.

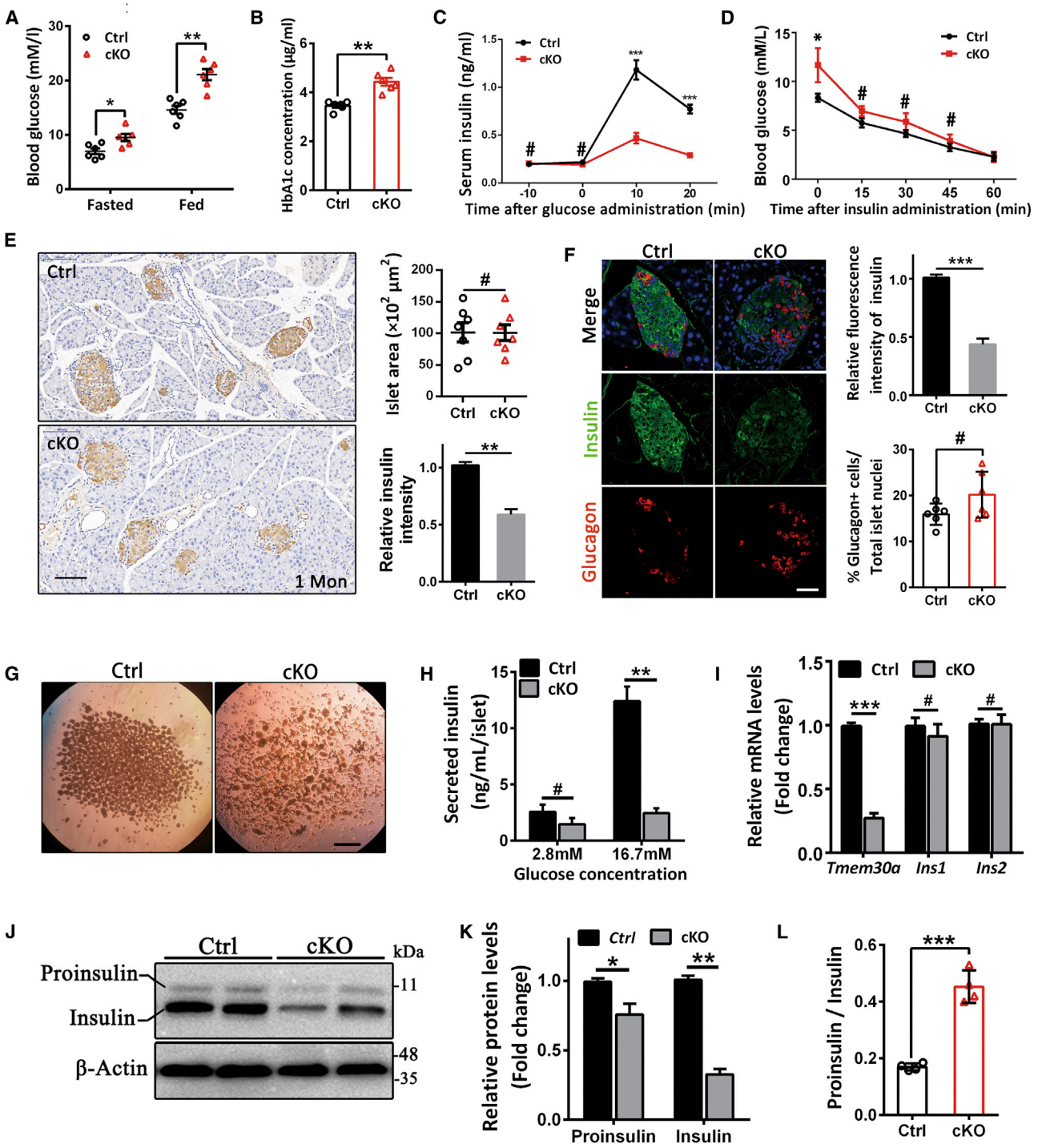

Figure 2. One-month-old *Tmem30a* cKO mice are hyperglycemic and have reduced levels of insulin expression

(A) Fasting (4-h fast) and fed blood glucose levels in 1-month-old chow-fed male control and cKO mice. Each point represents a glucose measurement from an individual animal (n = 6 for all groups). (B) HbA1c concentrations in 1-month-old control and cKO mice. Each point represents a HbA1c measurement from an individual animal. (n = 6). (C) Serum insulin levels in 1-month-old control (n = 6) and cKO (n = 8) mice during IPGTT. (D) Serum blood glucose levels in 1-month-old control (n = 6) and cKO (n = 8) mice during IPITT (intraperitoneal [i.p.] administration of 0.75 U insulin/kg body weight). (E) DAB staining for insulin in pancreatic section from 1-month-old control (left, upper panel) and *Tmem30a* cKO (left, lower panel) mice (n = 6), showing normal islet area (right, upper graph) but reduced insulin content (right, lower graph, normalized to control) in *Tmem30a* cKO β cells. (F) Immunofluorescent labeling of pancreatic cryosections from 1-month-old control and cKO littermates (n = 6) for insulin (green) and glucagon (red).

(legend continued on next page)

To assess whether *Tmem30a* deficiency affects development of islets, histological examination was performed in neonatal cKO mice at P6 and manifested a normal morphology of cKO islet compared to control, while the insulin content was decreased (Figures S9A and S9B). PDX1, ki67 immunostaining, and TUNEL assay also revealed no difference in differentiation, proliferation, and apoptosis of β cells in neonatal cKO islets (Figure S9C–S9E).

Heterozygous *Tmem30a*$^{loxP/+}$*; Ins2-Cre* mice were also tested here. Although IPGTT results from the heterozygous mice were slightly higher than from controls (Figures S10C and S10D), the two groups were comparable in terms of body weight, fasting blood glucose levels, insulin secretion, and insulin sensitivity (Figures S10A, S10B, S10E, and S10F).

To investigate the effect of sex hormones on metabolism in female experimental mice, phenotypic analysis of female mice was also performed in this study. Compared to controls (*Tmem30a*$^{loxP/loxP}$), female cKO mice were viable and fertile, yet exhibited hallmarks of T2DM, including obesity, glucose intolerance, and hyperinsulinemia from 2 months old (Figures S11A–S11F and S11I–S11L) and developed insulin resistance at 12 months old (Figure S11L). Histologic sections of pancreas from female cKO mice manifested islet hyperplasia, accompanied by disorganized α cells and decreased insulin intensity at both ages (Figures S11G, S11H, and S11M–S11P), in line with the diabetic phenotypes observed in age-matched male cKO mice.

It has been shown that Ins2-Cre transgenic mice might spontaneously develop glucose intolerance and impaired insulin secretion, due to its additional expression in the hypothalamus. To exclude this possibility, we introduced AgRP-IRES-Cre transgenic mice, which exert recombinase activity in eating-stimulating hypothalamic AgRP cells.[35] To directly confirm that the diabetic phenotype was derived from *Tmem30a* ablation instead of potential influence of transgene elements, we further generated another *Tmem30a* β cell-KO mouse line by crossing Pdx1-Cre mice with *Tmem30a*$^{loxP/loxP}$ mice (Figure S12A). Similar to *Tmem30a* cKO mice (Ins2-Cre-mediated), Pdx1-Cre-driven *Tmem30a* KO mice (pKO) also exhibited obesity, glucose intolerance, impaired insulin secretion, insulin resistance, and islet hyperplasia (Figures S12B–S12K). In addition, phenotypic analysis of heterozygous Ins2-Cre mice (*Cre*/+) were also tested, which indicated that their glucose metabolism did not differ from that of their wild-type littermates (+/+) at 6 months of age (Figure S13). These results suggest that the diabetic phenotype of *Tmem30a* cKO mice is a result of *Tmem30a* deficiency rather than the Cre activity in the hypothalamus.

Tmem30a deletion results in impaired insulin processing and secretion

Having demonstrated the severe glucose metabolism disorder in aging *Tmem30a* cKO mice, we next sought to uncover the primary mechanism underlying the diabetic phenotype observed in these animals. To this end, we analyzed 1-month-old mice, which exhibited normal body weight but showed the onset of hyperglycemia. Relative to controls, the blood glucose level of 1-month-old cKO mice was slightly elevated after overnight fasting but showed a greater absolute increase after consumption of regular chow (Figure 2A). The serum concentration of hemoglobin A1C (HbA1c), which reflects overall glycemic state, was also higher in 1-month-old cKO mice compared to controls (Figure 2B). The GSIS test revealed that while 1-month-old cKO and control mice had comparable basal insulin levels, much less insulin was released in response to glucose stimulation in cKO mice than in control littermates (Figure 2C). However, the results from the IPITT indicated that cKO mice displayed similar levels of insulin sensitivity to controls (Figure 2D), suggesting that the disruption of glycemic homeostasis in young cKO mice is mainly due to a defect in insulin production or secretion, rather than impaired insulin sensitivity of peripheral tissues.

In order to further explore insulin synthesis and secretion, we next examined pancreatic insulin expression in 1-month-old mice using immunohistochemistry. While we found that the overall morphology and size of islets from cKO mice were indistinguishable from those of the control animals (Figure 2E), insulin intensity was distinctly lower in *Tmem30a* cKO than in control β cells (Figure 2E). This finding was confirmed by coimmunostaining with antibodies against insulin and glucagon: a 60% decrease in insulin staining intensity compared to that of controls was observed in cKO islets (Figure 2F). Moreover, there was no significant difference in the proportion of α cells relative to controls (Figure 2F), excluding the contribution of glucagon to hyperglycemia.

Since glucose homeostasis and insulin secretion are regulated by multiple factors *in vivo*, islets were isolated and the cellular mechanisms potentially responsible for the observed decrease in insulin content were explored. Remarkably, the isolated *Tmem30a* cKO islets were more fragmented and vulnerable compared to control islets subjected to the same procedure of islet isolation (Figure 2G). We then collected the same number of unbroken islets from control and cKO mice and used them for the GSIS test. Consistent with the GSIS results obtained from 1-month-old mice *in vivo*, the insulin released from 1-month-old *Tmem30a* cKO islets was significantly reduced upon stimulation with 16.7 mM glucose relative to age-matched controls, although

The cKO islets showed diminished insulin expression (right, upper graph, normalized to control), while the percentage of glucagon-positive α cells was unchanged between control and cKO mice. (G) Images of isolated islets from 1-month-old control and cKO mice. Scale bar: 50 μm. (H) Insulin secretion from primary isolated islets from 1-month-old male control and cKO mice following glucose stimulation. (n = 8). (I) Relative (normalized to control) mRNA levels of *Tmem30a*, *Ins1*, and *Ins2* in isolated islets from control and cKO mice as assessed by qPCR (n = 8). (J) Western blotting analysis of insulin and proinsulin protein levels in islets from 1-month-old control and cKO mice (n = 6). (K) Both proinsulin and insulin levels (normalized to control) in islets from cKO mice were reduced compared with levels in control mice. (L) The ratio of proinsulin to insulin was elevated in islets from cKO mice relative to controls. *Tmem30a*$^{loxP/loxP}$ mice were used as controls. Student's t test was used for (A)–(F) and (H), and Mann-Whitney U test was used for (I), (K), and (L). *$p < 0.05$; **$p < 0.01$; ***$p < 0.001$. #, not significant. Data are presented as the means ± SEM.

there was no significant difference in basal insulin secretion between *Tmem30a* cKO and control islets (Figure 2H). Moreover, in agreement with the immunostaining data, western blot revealed that the intracellular proinsulin and insulin protein levels were significantly decreased in the *Tmem30a* cKO islets (Figures 2J and 2K), suggesting that the impairments in GSIS may be due to decreased insulin synthesis. In contrast, the ratio of proinsulin/mature insulin was elevated in *Tmem30a* cKO islets relative to that of controls (Figure 2L), indicating that while there was a decrease in overall levels of proinsulin and insulin, there was a relative accumulation of unprocessed proinsulin. In addition, the expression levels of *Ins1* and *Ins2* were unaltered in *Tmem30a* cKO islets (Figure 2I), suggesting that the reduced protein levels of proinsulin and insulin in these animals are not due to downregulation of insulin transcription but rather impairments in insulin maturation or secretion.

Tmem30a cKO β cells release excess proinsulin due to impaired insulin processing

Since an increased ratio of proinsulin to mature insulin was observed in isolated cKO islets, we next assessed the levels of plasma proinsulin following glucose stimulation using ELISA. 1-month-old *Tmem30a* cKO mice exhibited elevated plasma proinsulin concentrations in both basal and glucose-stimulated conditions compared with controls (Figure S14A). Consequently, the relative ratio of serum proinsulin to insulin was elevated in *Tmem30a* cKO mice compared to that of control mice (Figure S14B). For 4-month-old cKO mice, which had presented severe islet hyperplasia, basal plasma proinsulin levels were nearly 6-fold higher than those in controls, accompanied by a sharp increase in circulating proinsulin levels following glucose stimulation compared to controls (Figure S14C). As a result, the ratio of basal plasma proinsulin to insulin was significantly elevated and became more pronounced after glucose stimulation (Figure S14D), suggesting that increased levels of inactive proinsulin are released from *Tmem30a* cKO islets. The excess release of inactive proinsulin could potentially be explained by compensatory β cell proliferation and/or increased islet secretory capacity. Thus, the increased circulating proinsulin level and proinsulin-to-insulin ratio in *Tmem30a* cKO mice suggest that insulin maturation may be compromised in these animals. We therefore evaluated the status of insulin processing in *Tmem30a* cKO animals by analyzing the level of c-peptide, the cleavage product of proinsulin processing and an indicator of insulin processing, in β cells. Immunohistochemical analysis revealed a reduction in c-peptide levels in β cells of 1-month-old cKO mice compared with controls (Figures S14E and S14F), supporting the hypothesis that *Tmem30a* is required for normal insulin processing. Taken together, these data indicate that the elevated levels of circulating proinsulin in cKO mice may result from impaired conversion of proinsulin to insulin in the absence of *Tmem30a* and prompted us to further explore the role of *Tmem30a* in insulin maturation.

Tmem30a is required for insulin maturation and secretion from the TGN

The TGN is responsible for the packaging of proinsulin into ISGs and the subsequent conversion of ISGs to mature secretory granules, which are also morphologically termed DCVs. Given that our findings suggested impaired conversion of proinsulin to insulin in *Tmem30a* cKO mice, transmission electron microscopy (TEM) was next employed to examine potential subcellular changes related to the maturation and secretion of insulin granules in these animals. A striking reduction in the number of mature insulin-containing DCVs was observed in β cells of cKO mice (Figures 3A1, 3A2, and 3B), and swollen mitochondria were apparent throughout the cytoplasm (Figures 3A1 and 3A2), indicative of cell stress. The Golgi apparatus, where ISGs are formed, was also severely distended and surrounded by vacant vacuoles in *Tmem30a* cKO animals (Figures 3A3 and 3A4), implying the stress condition of the Golgi apparatus, which accounts for the observed defects in insulin maturation and the reduced number of DCVs. In addition, we also found that *Tmem30a* cKO β cells present enlarged ER (Figures 3A5 and 3A6), which may contribute to the reduction in protein levels of proinsulin and insulin, given the central role of the ER in insulin maturation. In contrast, the proportion of empty vesicles and the size of DCVs, as well as the dense core intensity (abundance of DCVs), were similar between *Tmem30a* cKO and control β cells (Figures 3C–3E).

To further investigate the cellular mechanisms governing insulin biosynthesis, we knocked down (KD) *Tmem30a* expression by lentivirus-mediated *Tmem30a* short hairpin RNA (shRNA) in mouse pancreatic β cell line MIN6 cells coupled with lentivirus-mediated GFP expression. We detected strong GFP fluorescence, indicating the high efficiency of lentiviral transduction in this cell line (Figure S15A). The *Tmem30a* expression level was decreased by 90% after the introduction of *Tmem30a*-shRNA compared with the negative control (Figure S15B). Consistent with the GSIS results obtained from the cKO islets, stimulation with 16.7 mM glucose resulted in significantly lower insulin levels in *Tmem30a* KD MIN6 cells than in control cells (Figure 4A). Immunocytochemical staining with a pan-insulin antibody (which detects both proinsulin and mature insulin) revealed that insulin was more concentrated in the Golgi apparatus of *Tmem30a* KD MIN6 cells than in the control cells (Figures 4B and 4C). This observation suggests that reduced levels of *Tmem30a* may prevent the budding of immature granules from the Golgi apparatus, which accounts for decreased levels of mature insulin in *Tmem30a* KD cells. Moreover, relative to control cells, *Tmem30a* KD MIN6 cells showed decreased protein levels of both proinsulin and insulin (Figures 4D and 4E), yet an increased ratio of proinsulin to mature insulin (Figure 4F), suggesting defective insulin maturation.

To validate this observation, we next performed rescue experiments for *Tmem30a* KD cells using constructed shRNA-resistant cDNA for *Tmem30a* (resTmem30a). Silent mutations were introduced in hemagglutinin (HA)-tagged *Tmem30a* to render it resistant to shRNA-mediated ablation of *Tmem30a* levels. MIN6 cells were transfected with control shRNA (shCtrl), or co-transfected with *Tmem30a*-specific shRNA (KD), along with empty vector or shRNA-resistant *Tmem30a* expression vector. Western blot analysis revealed that while shTmem30a completely knocked down the

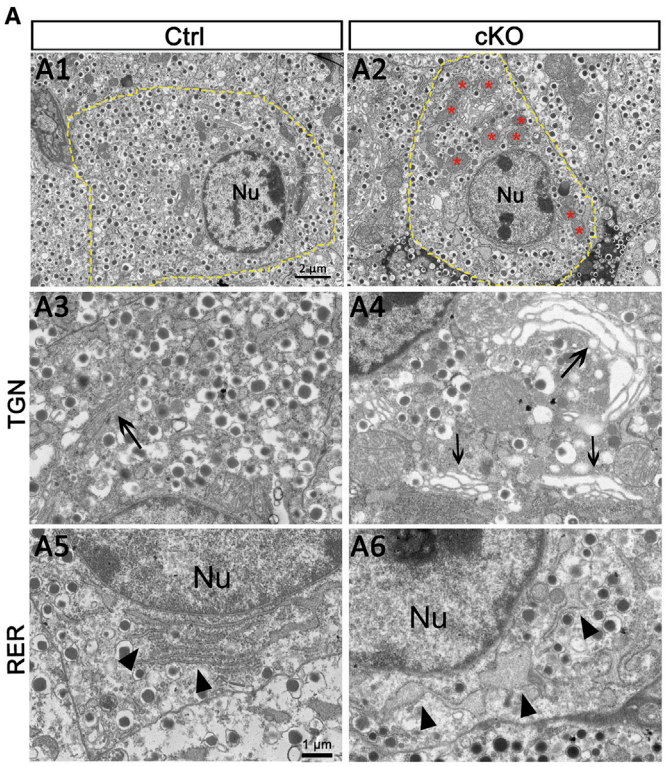

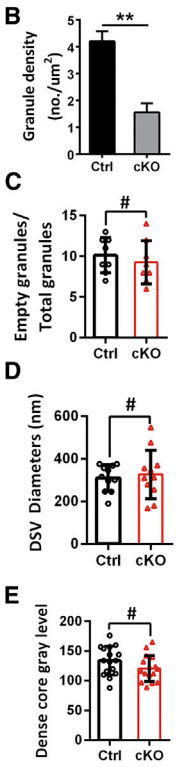

Figure 3. *Tmem30a* cKO β cells show swollen organelles and reduced density of mature insulin granules

(A) Representative transmission electron microscope (TEM) images of β cells in 1-month-old control and cKO mice (n = 5). Scale bar: 2 μm. The red asterisks in A2 indicate swollen mitochondria around the nucleus (Nu). A3 and A4 show the trans-Golgi network (TGN; arrows). A5 and A6 show the rough endoplasmic reticulum (RER; arrowheads). (B) Quantification of the density of insulin granules per β cell in control and *Tmem30a* cKO β cells (n = 6). (C) Quantification of the ratio of empty granules to total granules per β cell in control and cKO mice (n = 6). (D and E) Quantification of the diameter (D) and gray level of the dense core (E) of insulin granules in control and cKO mice. (n = 11 for D and n = 15 for E). *Tmem30a*$^{loxP/loxP}$ mice were used as controls. Student's t test was used for (B)–(E), and Mann-Whitney U test was used for (A). **p < 0.01; #, not significant. Data are presented as the means ± SEM.

expression of *Tmem30a*, *resTmem30a*-added KD cells expressed comparable levels of TMEM30A protein relative to shCtrl (Figures 4G and 4H). Importantly, insulin content and the ratio of proinsulin/insulin were also completely rescued by resTmem30a (Figure 4I). GSIS testing indicated that the insulin release was suppressed by shTmem30a compared to control cells and can be rescued by resTmem30a (Figure 4J), highlighting the vital roles of *Tmem30a* in insulin maturation and secretion.

Tmem30a is required for clathrin-dependent vesicle secretory and endocytosis pathways

Yeast flippases are known to be involved in clathrin-dependent transport between the TGN and PM, and clathrin and AP1+2 initiate assembly of the TGN- and PM-derived clathrin-coated vesicles.[36] Therefore, we next examined the expression and distribution of clathrin and AP1+2 in *Tmem30a* KD MIN6 cells. Immunoblotting analysis indicated that protein levels of both clathrin and AP1+2 were decreased in *Tmem30a* KD MIN6 cells relative to control cells (Figures 5A and 5B). Immunofluorescence staining revealed that clathrin expression tended to be more restricted to the Golgi complex in *Tmem30a* KD MIN6 cells than in controls (Figures 5C and 5D), suggesting the potential blockage of clathrin-coated vesicle exit. Considering we observed a similar pattern of insulin expression in the Golgi (Figures 4B and 4C), it is plausible that decreased expression of *Tmem30a* leads to impairments in the formation of DCVs and in insulin maturation by blocking the exit of clathrin-coated granules from the TGN.

Clathrin associated with adaptor proteins (APs) mediates multiple transport pathways between the TGN, endosomes, and the PM, which collectively initiate cellular endocytosis and exocytosis. In view of the fact that endocytosis and exocytosis are tightly coupled in β cells, we next examined the effect of Tmem30a depletion on clathrin-mediated endocytosis by monitoring the uptake of Alexa-594-conjugated transferrin, an endocytic marker, in MIN6 cells (Figure S16A). In this assay, initial binding of transferrin (50 μg/mL) was performed on serum-starved cells at 4°C to synchronize, followed by washing and warming at 37°C to trigger endocytosis. As expected, transferrin was rapidly internalized at 5 min by control cells. In contrast, only a small amount of transferrin was internalized by *Tmem30a* KD cells. Indeed, when both control and *Tmem30a* KD cells appeared to reach maximum internalization (at 30 min), the fluorescence intensity of cellular transferrin in *Tmem30a* KD cells was significantly lower than that of control cells (Figures S16A and S16C), despite similar overall levels of transferrin receptor (TfR) (Figure S16B), suggesting diminished transferrin internalization in *Tmem30a* KD cells. These data indicate that when *Tmem30a* is depleted, both clathrin-mediated secretory granule budding and endocytosis are compromised.

Tmem30a-deficient β cells show defective Glut2 transport and blunt Glut2-mediated glucose responses

Glut2, a major glucose transporter expressed in β cells that acts as the initiator of the GSIS response, is rapidly transported to the cell surface via clathrin-coated vesicles.[37] Since clathrin-mediated vesicular trafficking was impaired in *Tmem30a* KD cells (Figure 5), we hypothesized that Glut2 transportation to the PM might also be affected. To address this hypothesis, sections of the pancreas were prepared from 3-week-old *Tmem30a* cKO mice that did not yet exhibit a hyperglycemic phenotype. These sections were then immunostained with an antibody specific to Glut2. A marked reduction in Glut2 expression at the cell

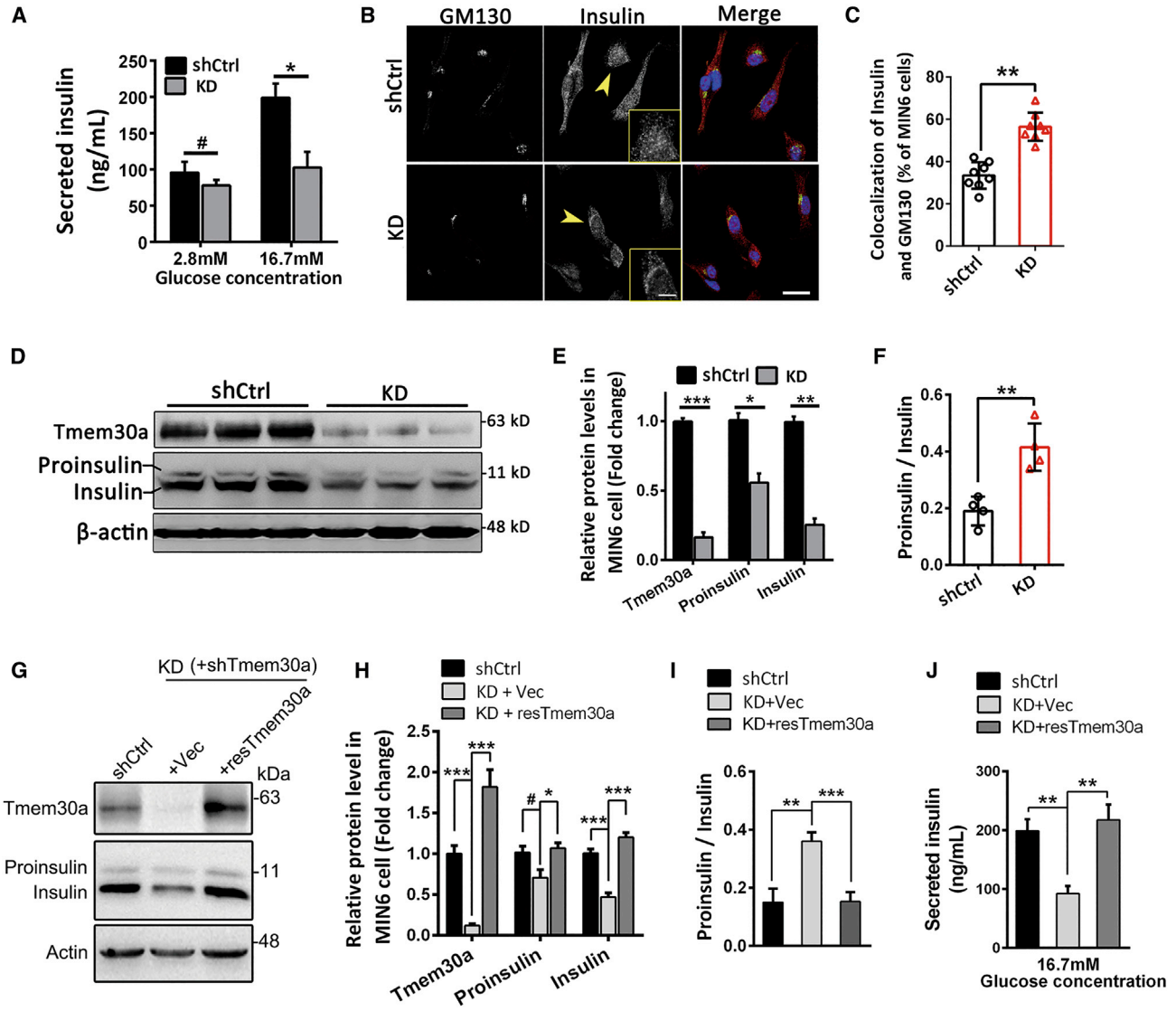

Figure 4. *Tmem30a* silencing impairs insulin maturation and secretion

(A) Insulin secretion from negative control (shCtrl) and *Tmem30a* knockdown (KD) MIN6 cells following stimulation with low glucose (2.8 mM) and high glucose (16.7 mM) (n = 8). (B) Control and *Tmem30a* KD MIN6 cells stained for GM130 (Golgi label) and insulin. Scale bar: 20 μm. The yellow arrowheads signify the subcellular localization of insulin; higher-magnification images are shown in the right bottom. Scale bar: 10 μm. (C) Percentage of insulin-positive cells that colocalized with GM130 (Golgi) in control and KD MIN6 cells. (D) Western blot showing proinsulin and insulin protein expression in control and KD MIN6 cells. (E) Both proinsulin and insulin levels in MIN6 cells were reduced compared with levels in control mice when Tmem30a was removed from MIN6 cells, while (F) the ratio of proinsulin to insulin was elevated. (n = 7). (G) shTmem30a-resistant cDNA (resTmem30a) was created by introducing silent mutations in HA-tagged Tmem30a to render it resistant to shRNA-mediated knockdown of *Tmem30a* protein levels. MIN6 cells were co-transfected with *Tmem30a*-specific shRNA, along with empty vector (Vec) or shRNA-resistant *Tmem30a*. Control shRNA transfected into MIN6 cells served as shControl (shCtrl). Western blot showing *Tmem30a* and insulin protein levels in shCtrl, vector-added, and resTmem30a-added KD MIN6 cells. (H) Both proinsulin and insulin levels in *resTmem30a*-rescued KD MIN6 cells were elevated compared with the levels in vector-added KD cells, and (I) the ratio of proinsulin to insulin was reduced to the normal level as shCtrl. (n = 3). Student's t test was used for (A) and (C), and Mann-Whitney U test was used for (E), (F), (H), (I), and (J). *p < 0.05; **p < 0.01; ***p < 0.001; #, not significant. Data are presented as the means ± SEM.

surface in *Tmem30a* cKO β cells was observed (Figure 6A). Furthermore, western blot analysis of MIN6 cell lysate showed a 50% reduction in the level of glycosylated mature Glut2 in *Tmem30a* KD cells relative to control cells, while no difference was observed in nonglycosylated Glut2 (Figures 6C and 6D). Since Glut2 is N-glycosylated in the Golgi apparatus prior to trafficking to the PM, our findings suggest that the reduced levels of glycosylated mature Glut2 likely resulted from the dysfunction of the Golgi apparatus in *Tmem30a*-deficient cells.

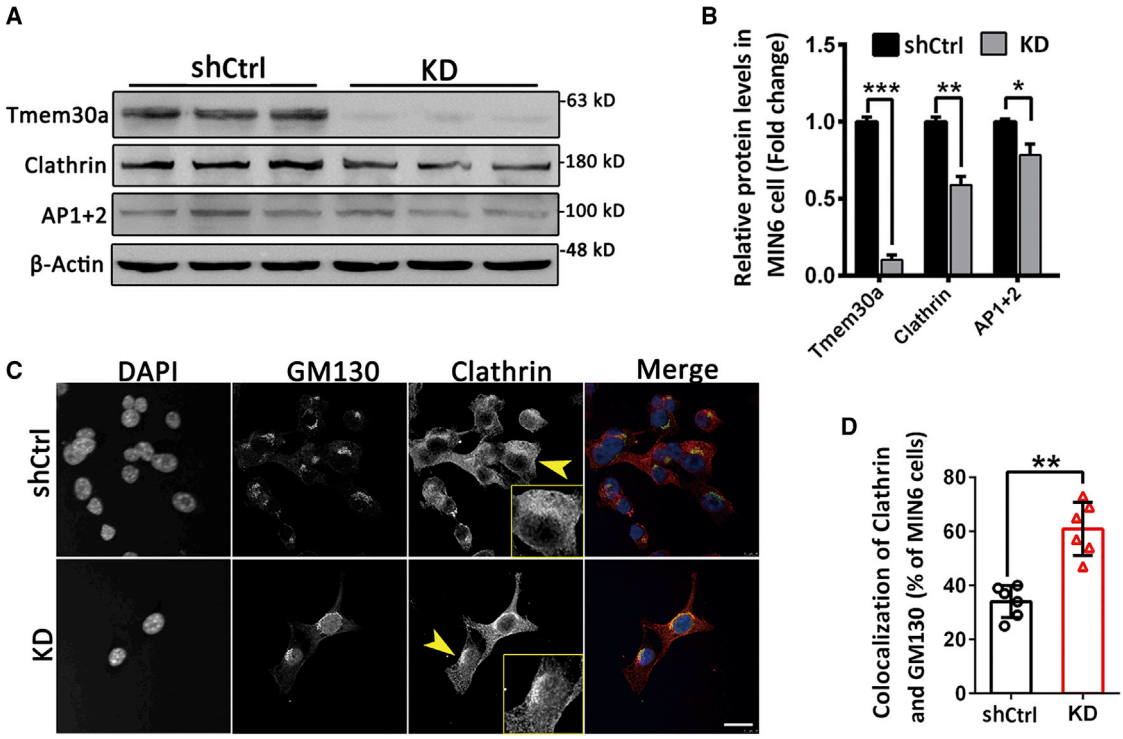

Figure 5. Tmem30a is required for clathrin-mediated vesicle trafficking

(A) Western blot showing expression of representative clathrin-related proteins (clathrin and AP1+2) in control and *Tmem30a* KD MIN6 cells. (B) Relative protein expression of Tmem30a, clathrin, and AP1+2 (normalized to control) in control and KD MIN6 cells. (n = 9). (C) Immunohistochemistry labeling GM130 (green), clathrin (red), and nuclei (DAPI, blue) in control and KD MIN6 cells. (n = 6). Scale bar: 10 μm. (D) Percentage of clathrin-positive cells that colocalize with GM130 (Golgi) in control and KD MIN6 cells. Student's t test was used for (B) and (D). *p < 0.05; **p < 0.01; ***p < 0.001. Data are presented as the means ± SEM.

The transcription factor PDX1 plays critical roles in β cell homeostasis and insulin secretion through its regulation of *Glut2* and *insulin* gene transcription.[38] Both immunofluorescence staining and western blot for PDX1 showed similar expression levels in control and cKO islets (Figures 6B–6D), suggesting that the decreased expression of mature Glut2 is mainly due to transport defects rather than endogenous hyperglycemia-induced downregulation of PDX1 expression.

To further assess the cellular transportation of other proteins that can regulate glucose homeostasis, two typical membranal ion channels (Kir6.2 and Cav1.2) were selected and examined using immunohistochemistry. Sections of the pancreas were prepared from 5-month-old *Tmem30a* cKO mice, which were then coimmunostained with insulin and an antibody specific to Kir6.2, the alpha subunit of the ATP-sensitive potassium channel in β cells.[39] Compared with that of control (expressed throughout cytosol), the expression level of Kir6.2 was significantly reduced in cKO β cells and showed an aggregation pattern in cytoplasm (Figure S17A), similar to the abnormal cellular localization of insulin in KD MIN6 cells (Figure 4B). Similarly, we also observed a significant downregulation in level of Cav1.2 (Figure S17B), the principal L-type voltage-gated calcium channel in β cells.[40] These data suggested that *Tmem30a* depletion could not only cause the defective Glut2 transport but also affect the transport of other GSIS-related proteins in β cells.

We next evaluated the cellular events underlying GSIS, including membrane depolarization and Ca^{2+} influx by activation of voltage-dependent calcium channels. Whole-cell patch-clamping revealed that KD cells showed a depolarized resting membrane potential relative to controls. Moreover, while 16.7 mM glucose stimulation of control cells resulted in a depolarization, KD cells did not show a change in membrane potential in response to elevated glucose levels (Figures 6E and 6F). To determine whether depolarization-dependent calcium influx was also affected by *Tmem30a* deficiency, we measured intracellular Ca^{2+} levels by loading MIN6 cells with a fluorescent calcium indicator and recording the change in fluorescence intensity. The Ca^{2+} influx evoked by a glucose challenge was significantly compromised in *Tmem30a* KD cells (Figures 7G and 7H). This impaired Ca^{2+} response may result from the decreased expression of Glut2 on the membrane, which in turn disrupts Ca^{2+}-dependent insulin exocytosis. Thus, our findings suggest that the GSIS impairment in *Tmem30a* cKO mice should arise from both defective ISG budding from the TGN and a blunted Glut2-mediated glucose sensing, highlighting the vital roles of *Tmem30a* in both insulin secretion and glucose sensing in pancreatic β cells.

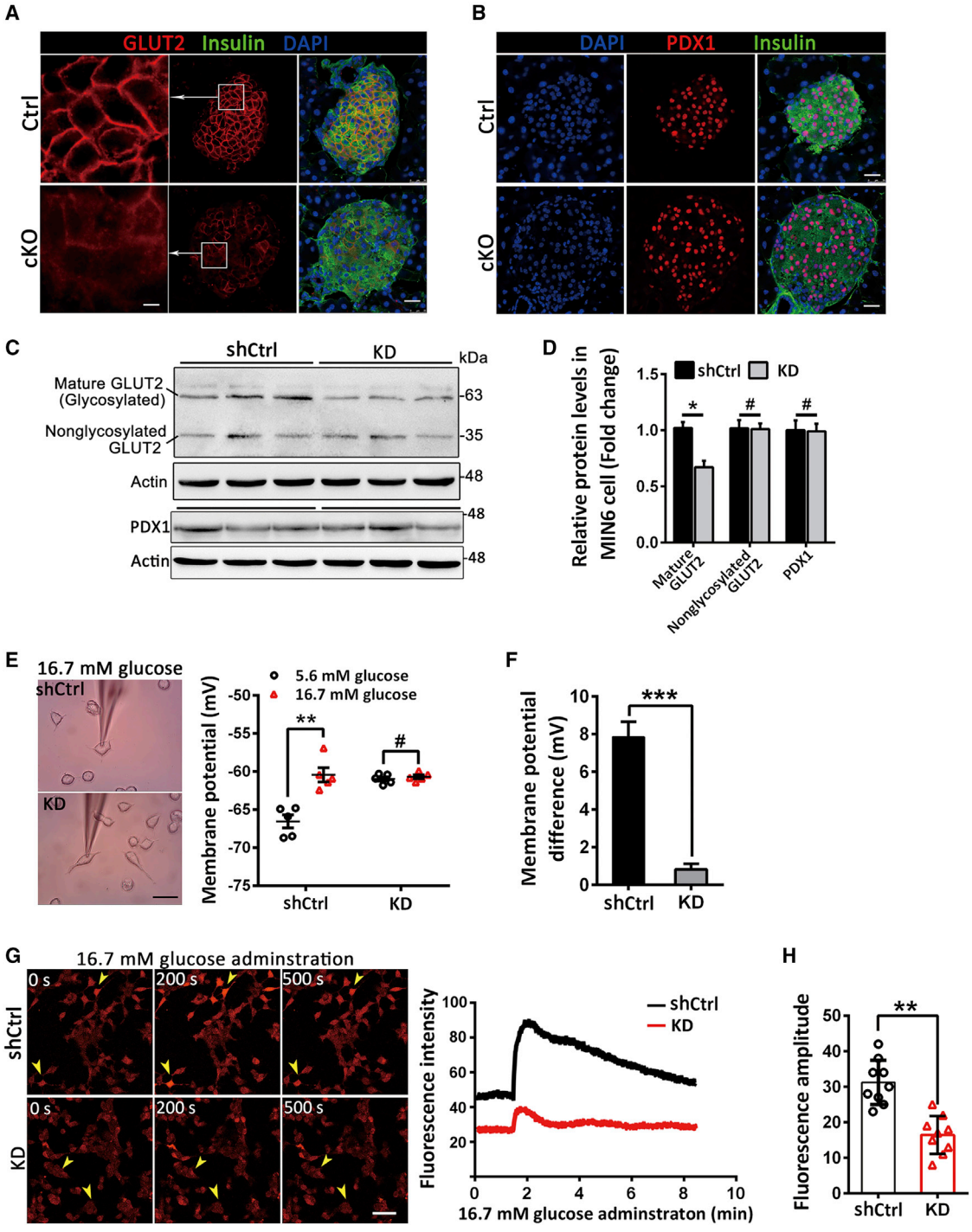

Figure 6. *Tmem30a* deficiency leads to impaired glucose sensing by reducing the expression of mature Glut2

(A) Immunohistochemistry labeling of GLUT2 (red), insulin (green), and nuclei (DAPI, blue) in pancreatic sections from 1-month-old control and *Tmem30a* cKO mice. Scale bar: 25 μm. Higher-magnification images of GLUT2 are shown in the leftmost panel of each row. Scale bar: 10 μm. (B) Immunohistochemistry labeling PDX1 (red), insulin (green), and nuclei (DAPI, blue) in pancreatic section from 1-month-old control and *Tmem30a* cKO mice. Scale bar: 25 μm. *Tmem30a*$^{loxP/loxP}$ mice were used as controls. (C) Western blot showing expression of GLUT2 and PDX1 proteins in control and *Tmem30a* KD MIN6 cells. β-actin was used as the loading control. (D) Relative (normalized to control) protein levels of mature GLUT2, nonglycosylated GLUT2, and PDX1 in control and Tmem30a KD MIN6 cells. (n = 5). (E and F) Resting membrane potential of control and *Tmem30a* KD MIN6 cells at 5.6 or 16.7 mM glucose concentrations. Scale bar: 25 μm. The amplitude of the depolarization of the membrane potential in response to

(legend continued on next page)

Tmem30a is responsible for asymmetric distribution of phosphatidylserine (PS) and determines subcellular localization of β cell-associated P4-ATPases

Tmem30a interacts with P4-ATPases to form a phospholipid flippase complex that mediates the rapid translocation of aminophospholipids from the outer leaflet to the inner leaflet of the PM, which in turn contributes to the initiation of vesicle formation. Accordingly, to investigate the effect of *Tmem30a* depletion on PS translocation across the membrane, the fluorescence-conjugated PS marker annexin-V was used to detect the distribution of PS in the outer layer of the PM without Triton permeabilization during the cellular block procedure. Compared to control cells, increased levels of annexin-V-labeled PS were observed on the outer membrane of *Tmem30a* KD MIN6 cells (Figures 7A and 7B), suggesting impaired PS flipping in conditions of *Tmem30a* deficiency. In line with this finding, Tmem30a depletion in MIN6 cells led to decreased NBD-labeled PS internalization and the PS translocase efficiency (reflected by median fluorescence intensity [MFI]) in KD MIN6 cells was reduced to 42.7% of control cells (Figures 7C and 7D), verifying the crucial role of Tmem30a on membranal PS flipping.

P4-ATPases are responsible for the translocation of PS from the exoplasmic to the cytosolic leaflet of cell membranes. To reveal the impact of Tmem30a deficiency on the expression pattern of interacting P4-ATPases in β cells, extracted mRNA from wild-type mouse pancreatic islets as well as MIN6 cells was subjected to qPCR after reverse transcription into cDNA. The qPCR data showed that *Tmem30a* is abundantly expressed in both mouse islets and MIN6 cells (Figures S18A and S18C). In mouse pancreatic islets, *Atp8b1*, *Atp89a*, *Atp11a*, *Atp8a1*, *Atp8a2*, and *Atp8b2* were expressed to different degrees (Figure S18A), and 5 of the 7 genes analyzed were expressed at lower levels in cKO mice than in control mice (Figure S18B). In MIN6 cells, *Atp8a1*, *Atp8b2*, *Atp9b*, *Atp10a*, and *Atp11b* were expressed to varying degrees (Figure S14C). When *Tmem30a* was silenced, *Atp8a1*, *Atp8b2*, *Atp10a*, and *Atp11a* showed reduced expression relative to their corresponding controls (Figure S18D).

To uncover the mechanism underlying the blockage of clathrin-mediated vesicle trafficking caused by *Tmem30a* depletion, we further investigated the effect of *Tmem30a* depletion on the subcellular localization of Atp8a1, Atp8b2, and Atp11a (which are expressed in both mouse islets and MIN6 cells) by immunofluorescence staining, using transiently transfected COS7 cells. In the absence of HA-tagged Tmem30a transfection, Flag-tagged Atp8a1, Atp8b2, and Atp11a exhibited a punctate distribution throughout the cytoplasm, with colocalization to calnexin-labeled ER (Figures 7E–7G, upper panel). In contrast, upon coexpression of Tmem30a, localization of Atp8a1 shifted to the GM130-labeled Golgi apparatus (Figures 7E and 7H), while ATP8B2 and ATP11A were located predominantly in the Golgi apparatus and partially on the PM (Figures 7F–7H). Intriguingly, the Golgi apparatus, where P4-ATPases are primarily located through the action of the Tmem30a subunit, is one of the sites from which clathrin-coated vesicles bud. Thus, the reduction in clathrin-mediated exocytic vesicle budding from the TGN caused by *Tmem30a* deficiency, which subsequently decrease DCV secretion and Glut2 transport, should result from the improper localization and reduced expression levels of P4-ATPases.

DISCUSSION

In this study, we demonstrated an important role for *Tmem30a* in insulin maturation and secretion, using extensive phenotypic and mechanistic analyses of *Tmem30a* cKO mice and *Tmem30a* KD MIN6 cells. We showed that TMEM30A associates with P4-ATPases to form the flippase complex that regulates the secretion of insulin granules from TGN. The TGN serves as the central sorting station of cells and is thus responsible for the proper targeting of newly synthesized secretory proteins toward their appropriate destinations. In the present work, we observed distended TGN cisternae by electron microscopy in *Tmeme30a*-depleted β cells (Figure 3A4), suggesting that *Tmem30a* is essential for proper function of the Golgi apparatus. Moreover, we observed an abnormal pattern of insulin and clathrin aggregation in the Golgi in *Tmem30a* KD MIN6 cells, implying an important function of *Tmem30a* in insulin budding events at Golgi.

In support of this view, we found that Atp8a1, Atp8b2, and Atp11a, when associated with Tmem30a, are largely located in the Golgi apparatus, with Atp8b2 and Atp11a additionally residing in the PM (Figures 7E–7H), indicating that their activity is tightly linked to vesicular trafficking to and from the PM. In eukaryotic cells, vesicular transport between the Golgi apparatus, endosomal system, and PM is mainly mediated by clathrin, which couples with many cofactors, such as APs, to form clathrin-coated vesicles. Our data show that loss of *Tmem30a* leads to decreased expression and incorrect subcellular localization of multiple P4-ATPases (Figures 7E–7H; Figures S18B and S18D), which in turn disrupts the formation of clathrin-coated vesicles and eventually affects bidirectional protein transport between the TGN and PM, such as the exocytosis of insulin granules. Thus, it can be concluded that the failure of clathrin-coated vesicle formation is the primary cause of impaired insulin release and glucose intolerance in *Tmem30a* cKO mice.

In addition, our study further indicated that the function and expression of Glut2, a critical glucose transporter expressed in the plasma membrane of β cells, were also affected in the absence of *Tmem30a*. However, unlike other glucose transporters, Glut2 is directly trafficked to the cell surface after N-glycosylation in the Golgi apparatus and subsequently undergoes rapid lysosomal degradation without

16.7 mM glucose is reduced in KD cells compared to controls. (n = 5). (G) Representative Ca^{2+} imaging examining the effect of glucose on the intracellular Ca^{2+} concentration measured by the Cal-590 fluorochrome. Both control and *Tmem30a* KD MIN6 cells were stimulated with 16.7 mM glucose, and changes in fluorescence were recorded. (H) Quantification of the fluorescence amplitude of Ca^{2+} influx evoked by a 16.7 mM glucose challenge in control and *Tmem30a* KD MIN6 cells. (n = 9). Student's t test was used for (H), and Mann-Whitney U test was used for (D)–(F). *p < 0.05; **p < 0.01; ***p < 0.001; #, not significant. Data are presented as the means ± SEM.

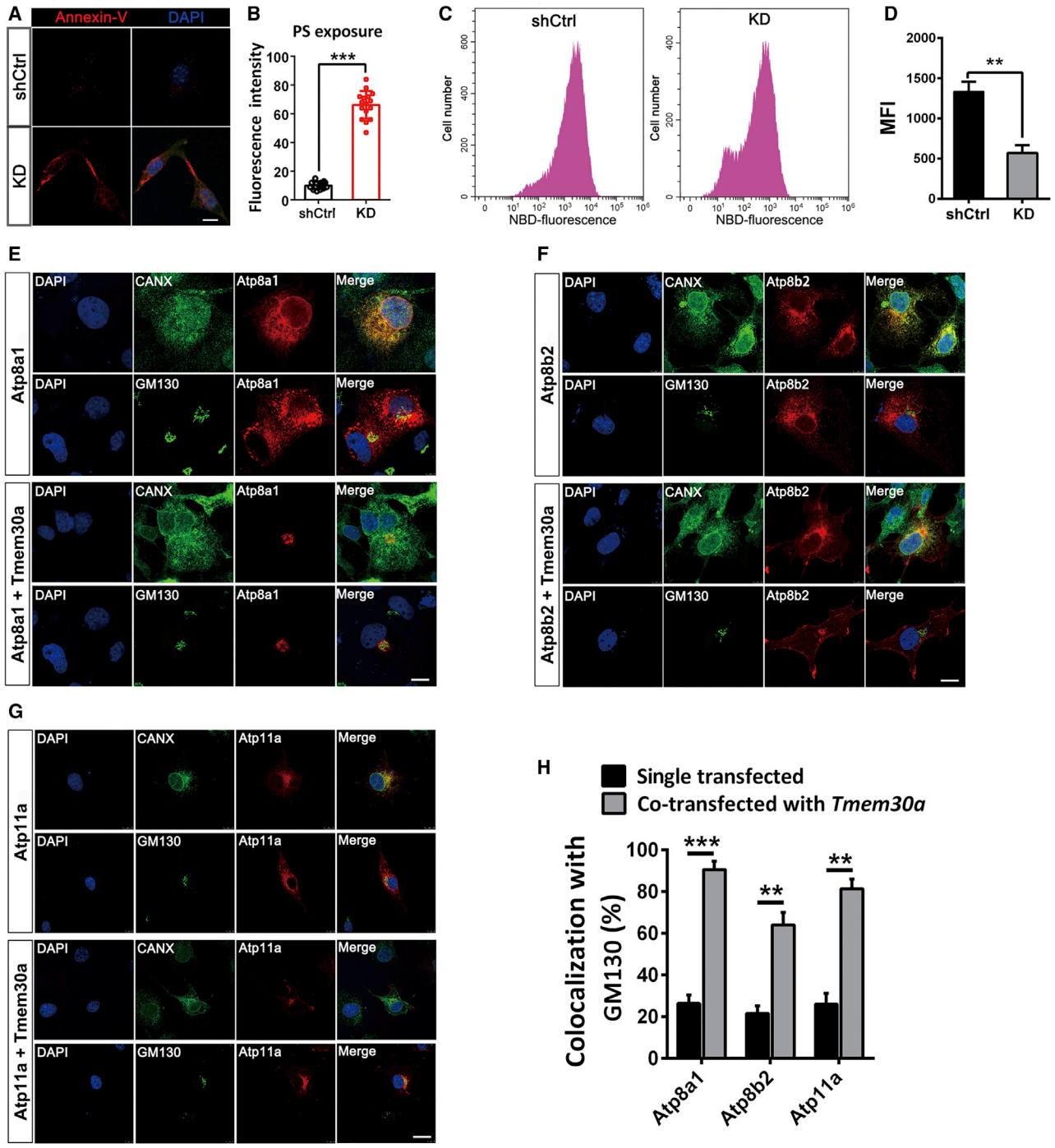

Figure 7. *Tmem30a* is responsible for asymmetric distribution of PS and determines subcellular localization of β cell-associated P4-ATPases

(A and B) Annexin V staining of control and KD MIN6 cells, showing high PS exposure on the *Tmem30a* KD MIN6 cell surface compared to control cells. (n = 12 cells). Scale bar: 20 μm. (C and D) Loss of *Tmem30a* led to decreased NBD-PS internalization (C). The y axis shows numbers of NBD-PS-labeled MIN6 cells. The x axis represents NBD-PS fluorescence intensity of intact living cells. KD MIN6 cells exhibited decreased NBD fluorescence intensity, compared to control cells (D) (n = 12). MFI, median fluorescence intensity. (E–G) Immunocytochemistry from COS7 cells transiently cultured in high glucose and transiently cotransfected with an expression vector for *Flag*-tagged *Atp8a1*/*Atp8b2*/*Atp11a* and an expression vector for N-terminally HA-tagged *Tmem30a*. After 48 h of transfection, cells were stained with anti-Flag antibody and anti-HA antibody with either the Golgi marker GM130 or ER marker calnexin (CANX). Scale bar: 20 μm. (H) Percentage of colocalization of transfected P4-ATPases (Atp8a1, Atp8b2, Atp11a) with GM130-marked Golgi in COS7 cells either transfected only with a P4-ATPase (single transfected) or co-transfected with a P4-ATPase and Tmem30a (n = 12). Student's t test was used for (B), (D), and (H). $^{**}p < 0.01$; $^{***}p < 0.001$; #, not significant. Data are presented as the means ± SEM.

recycling.[37] The balance between rapid cell-surface delivery and rapid degradation allows for an acute regulation of Glut2 protein levels. With this in mind, we conclude that the decreased levels of mature glycosylated Glut2 detected in *Tmem30a*-depleted MIN6 cells (Figures 6C and 6D) potentially resulted from deficits in Glut2 N-glycosylation at the TGN, highlighting a role for *Tmem30a* in maintaining Golgi-dependent glycosylation. Accordingly, diminished cell-surface expression and increased intracellular localization of Glut2 were observed in *Tmem30a* cKO β cells (Figure 6A). Considering that Glut2 transporter is essential for glucose sensing and subsequent cascade responses, such as blunted membrane depolarization and reduced calcium influx in response to glucose stimulation (Figures 6E–6H), our findings suggest that reduced Glut2 levels should also contribute to the pathogenesis of diabetes in these mutant mice.

P4-ATPases transport PS and, to a lesser extent, phosphatidylethanolamine (PE) from the outer to the cytoplasmic (inner) leaflet of the PM, as well as intracellular vesicles from the luminal leaflet to the cytoplasmic (outer) leaflet of the bilayer.[41] Several lines of evidence have suggested that unidirectional translocation of phospholipids catalyzed by P4-ATPases and their subsequent asymmetry help induce the membrane curvature that initiates vesicle budding from the TGN and PM.[8] Our data strengthen the possibility that the asymmetric distribution of PS maintained by flippases is required for vesicle formation, since *Tmem30a* cKO-induced downregulation and mislocalization of several P4-ATPases result in impaired PS flipping and a consequent defect in cellular trafficking events between TGN and PM. Thus, it is tempting to speculate that the flippase-catalyzed PS asymmetry at the budding sites of the TGN might also play fundamental roles in generating tightly curved transport vesicles. However, the mechanisms by which flippases mediate vesicle formation remain unclear. One possibility is that the P4-ATPases impart curvature to the membrane by shifting phospholipids to the cytosolic leaflet, thereby increasing the surface area of the cytosolic leaflet so that the clathrin coat can more easily deform.[8] Alternatively, it is also possible that the high concentration of negatively charged PS on the cytoplasmic surface of the TGN and PM provides a unique recruitment signal for vesicle-coated proteins with specific PS-binding domains, which induces vesicle biogenesis.[42]

There are 14 P4-ATPases in mammals, which are widely distributed across various tissues and cells, mediating normal vesicle trafficking between different membranous components. *Tmem30a* deficiency could cause dysfunction of most of interacting P4-ATPases. In the present study, we mainly explored the roles of TMEM30A in insulin secretion and GSIS response. Indeed, the maintenance of blood glucose homeostasis is a complicated process involving numerous molecules. The failure of flippase-dependent vesicle trafficking caused by *Tmem30a* depletion might extensively affect many other glucose-metabolism-related cellular processes and molecules in β cells, which together induce imbalance of blood glucose homeostasis and subsequent diabetic phenotype in cKO mice. However, the detailed underlying mechanisms of this process warrant further exploration.

One unique feature of our *Tmem30a* cKO model is that *Tmem30a* cKO mice develop severe diabetic complications spontaneously under normal chow diets, including obesity, IR, and hepatic phonotypes. It is recognized that obesity is an important basis for the occurrence of IR.[43] During the development of obesity, excessive free fatty acids (FFAs) can induce insulin resistance in insulin target cells. In addition, excessive proliferation of adipose cells causes macrophage infiltration and activation of chronic inflammatory response, which subsequently leads to cell stress and promotes IR occurrence.[44,45] In the present study, β cell dysfunction in cKO mice leads to compensatory islet hyperplasia, hyperinsulinemia, and metabolism disorders, which in turn caused obesity as well as excessive proliferation and volume increase of adipocytes (Figure 1), laying the basis for IR initiation. In addition, the cKO mice also developed severe hepatic lesions, including hepatic steatosis, cirrhosis, and hepatocarcinoma, in the late stages of the disease (Figure S3). In the C57L/6J genetic background, however, the leptin-deficient *ob/ob* mice display only mild functional and morphological changes; they have a limited lifespan and died before serious liver complications developed.[46] Although the precise mechanism under these diabetic complications and severe hepatic phenotypes in cKO mice remains unclear, we provide an excellent model for studying diabetes-related complications.

In summary, our study has revealed essential roles for *Tmem30a* in insulin production and glucose homeostasis. We show that *Tmem30a* deficiency causes β cell dysfunction and diabetes due to defects in granule budding at the TGN. These impairments in cellular trafficking in turn affect insulin maturation and glucose sensing in β cells, reflecting a central role of *Tmem30a* in clathrin-dependent vesicle transport through the regulation of P4-ATPase localization and function. Most importantly, the *Tmem30a* cKO mouse model closely mimics key characteristics of human T2DM patients. This mouse model is thus an invaluable tool in understanding the pathogenesis of T2DM and for treatment development.

MATERIALS AND METHODS

Materials availability

All unique/stable reagents generated in this study are available from the Lead Contact with a completed Materials Transfer Agreement.

Data and code availability

The published article includes all datasets generated or analyzed during this study.

Mouse model and genotyping

All animal experiment study protocols were approved by the Animal Care and Use Committee of Sichuan Provincial People's Hospital. All animals were housed in a temperature-controlled room (24°C) with a 12-h light/dark cycle and were fed a normal diet (diet 5001, LabDiet, St. Louis, MO, USA). Mice were maintained on a C57BL/6J background.

Mice with a *Tmem30a* deletion specifically in pancreatic β cells were generated as previously described.[17–22] Briefly, *Tmem30a*$^{loxP/loxP}$ mice

were crossed with *Tg(Ins2-Cre) 25Mgn* (also known as Rip-Cre, Jackson Laboratory, stock no. 003573) transgenic mice, to yield progeny with the genotype *Tmem30a*$^{loxP/+}$; *Ins2-Cre*. Then, the *Tmem30a*$^{loxP/+}$; *Ins2-Cre* mice were crossed to *Tmem30a*$^{loxP/+}$ animals to generate *Tmem30a*$^{loxP/loxP}$; *Ins2-Cre* (hemizygous) mice (*Tmem30a* cKO mice). The littermate mice were used as controls, and their genotype information was described in figure legends.

Tmem30a$^{loxP/loxP}$ mice were crossed with AgRP-IRES-Cre transgenic mice (Jackson Laboratory, stock no. 012899) to yield *Tmem30a*$^{loxP/loxP}$, *Agrp-Cre* mice (AgRP-KO), from which *Tmem30a* was excised in hypothalamic AgRP-expressing neurons. Meanwhile, *Tg(Pdx1-Cre*^{Tuv}*)* transgenic mice (Jackson Laboratory, stock no. 014647) was also introduced to produce *Tmem30a*$^{loxP/loxP}$, *Pdx1-Cre* mice (pKO). Both mouse models were used to rule out the possibility that the phenotypes resulted from the additional Ins2-Cre expression in the hypothalamus.

To monitor the expression pattern of the Cre enzyme, a tdTomato reporter gene was used (strain name: B6. Cg-Gt[ROSA]26Sortm14 [CAG-tdTomato]Hze/J; Jackson Laboratory, stock number 007914).[47] Mouse genomic DNA samples were extracted from mouse tails and genotyped using PCR. The floxed *Tmem30a* alleles and Ins2-Cre were genotyped using the corresponding primers (Table S1) at an annealing temperature of 58°C. The tdTomato mice were genotyped using primers provided by the JAX mouse service (Table S1). All amplification reactions were performed using a master mix (Invitrogen, Carlsbad, CA, USA) as per the manufacturer's instructions. The PCR products were separated by DNA electrophoresis on a 3% agarose gel.

Blood analysis

For the IPGTT, mice were fasted for 16 h and then injected intraperitoneally with 2 mg glucose per gram body weight. Blood was collected from the supraorbital vein. The concentration of blood glucose was measured by a glucometer (Roche, Basel, Switzerland) according to the manufacturer's instructions. For the IPITT, mice were fasted for 6 h and injected subcutaneously with 0.75 U human insulin (Novo Nordisk, Tianjin, China) per kilogram body weight, and the concentration of blood glucose was measured. For GSIS, fasted mice were injected intraperitoneally with 0.75 mg glucose per gram body weight. Blood samples were collected and separated from plasma by centrifugation at room temperature. Plasma insulin was measured using a mouse ultrasensitive insulin ELISA kit (cat. no. 90080, Crystal Chem, Elk Grove Village, IL, USA) according to the manufacturer's instructions. Similarly, plasma glucagon was measured using glucagon (cat. no. 81518, Crystal Chem) ELISA kits according to the manufacturer's instruction.

Whole-body metabolic analysis

Animals for metabolic parameter measurements were maintained with regular chow. Mice were individually placed in a PhenoMaster metabolic cage unit (IntelliCage, TSE Systems, Germany). Standard 12-h light (6 a.m. to 6 p.m.) and dark cycles (6 p.m. to 6 a.m.) were maintained throughout the experiment. Animals had free access to food and water and were allowed to adapt to the metabolic cage for 24 h prior to data collection. Then the volume of O_2 consumption and CO_2 production, respiratory exchange ratio, heat production, and locomotor activity were continuously recorded during the next 48 h according to the instructions of the manufacturer.

Cell culture and transfection

MIN6 cells were cultured in RPMI-1640 medium (Hyclone, South Logan, UT, USA) supplemented with 10% fetal bovine serum (Gibco, Grand Island, NY, USA), 100 U/mL penicillin/streptomycin (Invitrogen, Carlsbad, CA, USA) and 50 mM β-mercaptoethanol (Sigma, St. Louis, MO, USA) in an incubator set to 37°C with 5% CO_2. COS-7 cells were cultured in DMEM with high glucose (Hyclone, South Logan, UT, USA) supplemented with 10% fetal bovine serum (Gibco, Grand Island, NY, USA) and 100 U/mL penicillin/streptomycin (Invitrogen, Waltham, MA, USA) in an incubator set to 37°C with 5% CO_2. For immunocytochemistry, cells were seeded in 24-well plates (Corning, Corning, NY, USA) and transiently transfected with HA-tagged Tmem30a or Flag-tagged Atp8a1/Atp8a2/Atp11a using Lipofectamine 3000 (Invitrogen, Carlsbad, CA, USA) according to the manufacturer's instructions. Cells were harvested after 48 h.

RNA interference and rescue

Lentiviruses carrying shRNA targeting *Tmem30a* (5′-GAGTTGTACTGCTAGTAATTA-3′) and a negative control shRNA (5′-TTCTCCGAACGTGTCACGT-3′) were purchased (Genechem, Shanghai, China). *Tmem30a* lentiviral particles (2×10^7 TU/mL; MOI = 20) mixed in serum-free medium with transfection reagent were transfected into cultured MIN6 cells. The medium was replaced by RPMI-1640 medium after 12 h. Cells were harvested 72 h after transfection. For rescue experiments, shTmem30a-resistant cDNA (resTmem30a) was created by site-directed mutagenesis by introducing three silent mutations (G1032A, C1035T, and C1038T) within the shTmem30a target sequence (5′-GAGTTGTACTGCTAGTAATTA-3′). MIN6 cells were co-transfected by Tmem30a-specific shRNA (MOI = 20) together with shRNA-resistant Tmem30a (1 μg) to render it resistant to shRNA-mediated ablation of Tmem30a protein levels. All experimental procedures were performed strictly according to the protocols provided by the manufacturers.

CT scan analysis

As a measure of obesity, adipose tissue distribution was examined in mice using the LaTheta Micro-CT Scanner LCT-200 (Hitachi Aloka Medical, Tokyo, Japan) according to the manufacturer's protocol. CT scanning was performed at 2-mm intervals from the diaphragm to the bottom of the abdominal cavity.

Pancreatic islet isolation

Islets were isolated by the intraductal collagenase digestion technique. Briefly, mice were deeply anesthetized with a combination of ketamine (16 mg/kg body weight) and xylazine (80 mg/kg body weight). The common bile duct was anterogradely cannulated, and the pancreas was distended with collagenase (type IV) (Worthington).

The pancreas was harvested and digested by 1.5 mg/mL Collagenase P (Roche, Redwood City, CA, USA) for 30 min at 37°C. Islets were then isolated by generating a sedimentation gradient of histopaque 1077 (Sigma, St. Louis, MO, USA). Floating islets were washed, and unbroken islets of comparable size were hand-picked and then transferred into RPMI-1640 medium (Hyclone, South Logan, UT, USA) containing 10% fetal bovine serum and 100 U/mL penicillin/streptomycin (Invitrogen, Carlsbad, CA, USA) in an incubator set to 37°C with 5% CO_2. After overnight incubation, selected islets were equilibrated with Krebs Ringer buffer (KRB; 128 mM NaCl, 4.8 mM KCl, 1.2 mM KH_2PO_4, 1.2 mM $MgSO_4$, 2.5 mM $CaCl_2$, 5 mM $NaHCO_3$, 10 mM HEPES, and 0.1% BSA) containing 2.8 mM glucose for 30 min at 37°C. Then, islets were incubated in KRB containing 2.8 mM glucose for 1 h at 37°C. Next, islets were stimulated with KRB containing 16.7 mM glucose for 1 h at 37°C. The total insulin content of islets was harvested by overnight extraction in acid ethanol. Secreted insulin in the supernatant was measured by ELISA.

RNA isolation and quantitative RT-PCR analysis

Total RNA was isolated from mouse islets or MIN6 cells (TRIzol Reagent; Invitrogen, Carlsbad, CA, USA), and RNA concentrations were then quantified using an ND-1000 spectrophotometer (NanoDrop Technologies, Wilmington, DE, USA). Total RNA (1 μg) was converted into first-strand cDNA by reverse-transcription kit (Invitrogen, Carlsbad, CA, USA), and qPCR was performed using SYBR Green PCR Master Mix (Thermo Fisher Scientific, Waltham, MA, USA) and an ABI 7500 Fast Real-Time PCR System (Applied Biosystems, Foster City, CA, USA). The PCR conditions were 95°C for 10 min, followed by 42 cycles at 95°C for 15 s and 60°C for 45 s. The primer sequences used are shown in Table S1. Target gene expression was normalized relative to the expression of *GAPDH* or *β-actin*.

Histology and quantification

For H&E staining, deeply anesthetized animals were transcardially perfused with phosphate-buffered saline (PBS) followed by 4% paraformaldehyde (PFA) in 100 mM phosphate buffer (PB) (pH 7.4). Isolated tissues were fixed in 4% paraformaldehyde overnight at 4°C. Then, the fixed tissues were embedded in paraffin, cut into 5-μm sections, and stained using an H&E staining protocol. The area of fat cells and pancreas islets was quantified by Pannoramic Viewer 1.1 (3DHISTECH, Budapest, Hungary).

Immunohistochemistry

For immunohistochemistry, mice were anesthetized with a combination of ketamine (16 mg/kg body weight) and xylazine (80 mg/kg body weight) and perfused transcardially with PBS, followed by 4% paraformaldehyde in 100 mM PB (pH 7.4). The dissected tissues were immersed in 4% paraformaldehyde for 2 days at 4°C. Then, the pancreases were removed and dehydrated in 30% sucrose for 24 h. A tissue block containing the pancreas was next prepared and embedded in optimal cutting temperature (OCT) solution and sectioned at a thickness of 10 μm by Leica freezing slicer CM1520. The sections were blocked and permeabilized with 10% normal donkey serum and 0.2% Triton X-100 in PB for 2 h and then incubated overnight at 4°C with the primary antibodies. The primary antibodies were diluted in PBS containing 5% normal donkey serum and 0.2% Triton X-100 and used at concentrations as described in Table S2. The secondary antibodies were diluted in PBS containing 5% normal donkey serum and 0.2% Triton X-100 at 1:1,000 dilution. TUNEL analysis was performed using an *In Situ* Cell Death Detection Kit following the manufacturer's instructions (Roche, Redwood City, CA, USA). The images were captured using a Zeiss LSM 800 confocal scanning microscope. The fluorescence intensity and colocation ratio were measured by Zen software.

Immunocytochemistry

The transfected cells were fixed with 4% paraformaldehyde in 100 mM (pH 7.4) for 15 min at room temperature. After blocking with PBS containing 5% normal goat serum and 0.2% Triton X-100, cells were incubated with specific antibodies (Table S2) at 4°C overnight. The secondary antibodies comprised goat anti-rabbit Alexa 488, goat anti-rabbit Alexa 594, goat anti-mouse Alexa 488, goat anti-mouse Alexa 594, donkey anti-rat Alexa 488, and donkey anti-rabbit Alexa 633 (Invitrogen, Carlsbad, CA, USA, 1:500 dilution). Nuclei were counterstained with DAPI (cat. no. D8417, Sigma, St. Louis, MO, USA). Immunocytochemistry images were captured with a Zeiss LSM 800 confocal scanning microscope. The fluorescence intensity and colocation ratio were measured by Zen software.

Western blotting

Tissues or cells were lysed in radioimmunoprecipitation assay buffer containing a protease inhibitor cocktail (Roche, Redwood City, CA, USA) and a phosphatase inhibitor (Roche, Redwood City, CA, USA). The protein concentration of the lysates was determined using a DC Protein Assay as per the manufacturer's instructions (Bio-Rad, Hercules, CA, USA). Equal amounts of protein were separated on SDS polyacrylamide gels and transferred to polyvinylidene fluoride membranes (GE Healthcare, Chicago, IL, USA). The blots were blocked with 8% nonfat dry milk in Tris-buffered saline (TBS) solution with the detergent Tween 20 for 2 h at room temperature. Then, the membranes were incubated with the primary antibodies in blocking solution overnight at 4°C. The primary antibodies used for western blotting are shown in Table S2. The primary antibodies were detected with anti-mouse or anti-rabbit horseradish peroxidase (HRP)-conjugated secondary antibodies (1:5,000; Bio-Rad, Hercules, CA, USA), and the signal was developed using Supersignal West Pico Chemiluminescent Substrate as per the manufacturer's instructions (Pierce, Rockford, IL, USA). The relative intensity of the immunoreactive bands was quantified using the gel analysis tool provided in the ImageJ software. The intensity of the proteins of interest was normalized to that of GAPDH or β-actin.

TEM

Anesthetized mice were fixed by transcardial perfusion with PBS, followed by perfusion with 2.5% glutaraldehyde in cacodylate buffer. Tissues were postfixed in 2.5% glutaraldehyde in cacodylate buffer (pH 7.2) overnight at 4°C. The pancreases were dissected,

immersion-fixed with 4% paraformaldehyde for 8 h, and sectioned sagittally at 100-mm intervals using a vibratome. Sections were incubated in 1% osmium tetroxide for 1 h, washed in 0.1 M phosphate buffer, and dehydrated via an ascending series of ethanol and propylene oxide and embedded in Epon (25 g Epon 812, 13 g dodecenyl succinic anhydride [DDSA], 12 g nadic methyl anhydride [NMA], and 1 mL 2,4,6-Tris [dimethylaminomethyl] phenol [DMP-30], Electron Microscopy Sciences). Ultrathin sections (70 nm) were cut and stained with uranyl acetate and lead citrate. The sections were imaged under a Philips CM120 scanning transmission electron microscope.

Electrophysiological experiments

Prepared MIN6 cells were patch-clamped in conventional whole-cell configuration at 33°C–34°C. Experiments were performed using an Axopatch200B amplifier and a Digidata1440A Data Acquisition System (Molecular Devices, San Jose, CA, USA), in sampling frequency 5 kHz and filtering frequency 10 kHz. Patch pipettes were fabricated by a P97 micropipette puller using filament capillary glass (Sutter Instrument Company, Novato, CA, USA). Filamented patch pipettes had typical resistances of 3–5 megaohms when fire-polished and filled with an intracellular solution containing 140 mM KCl, 1 mM $MgCl_2$, 0.05 mM EGTA, 10 mM HEPES, and 5 mM MgATP (pH 7.3), with KOH. After the whole-cell configuration was established, the resting membrane potential (RMP) was measured in "I = 0" mode. Changes in membrane potential were calculated by the membrane potential difference of MIN6 cells between 16.7 and 5.6 mM glucose concentration.

Measurement of intracellular Ca^{2+} influx

The cytosolic Ca^{2+} concentration was assessed using the Ca^{2+} indicator Cal-590 AM (AAAT, Sunnyvale, CA, USA). All experimental procedures were conducted according to the product protocols. A 5 mM stock solution of Cal-590 AM esters in high-quality, anhydrous DMSO was prepared. On the day of the experiment, either Cal-590 AM was dissolved in DMSO or an aliquot of the indicator stock solution was thawed to room temperature. The Cal-590 AM working solution of 10 to 20 μM in Hanks and HEPES buffer (HHBS) with 0.04% Pluronic F-127 (AAAT, Sunnyvale, CA, USA) was prepared. Then, an equal volume of the dye working solution was added to the cell plate. The dye-loading plate was incubated in a cell incubator for 60 min and then incubated at room temperature for another 30 min. The dye working solution was replaced with HHBS or, if applicable, a buffer that contains an anion transporter inhibitor, such as 1 mM probenecid, to remove excess probes. The experiments were run at Ex/Em = 540/590 nm on a Zeiss LSM 800 confocal scanning microscope. The fluorescence intensity was measured by Zen software to determine the amount of intracellular Ca^{2+}.

Lipid translocation assay

Lipid translocation assay was performed as previously described.[48] The labeled phospholipid analog 16:0–06:0 NBD-PS (1-palmitoyl-2-[6-[(7-nitro-2-1,3-benzoxadiazol-4-yl)amino] hexanoyl]-sn-glycero-3-phospho-L-serine [ammonium salt]) were purchased from Avanti Polar Lipids (Alabaster, AL, USA). NBD-PS powder stocks were dissolved in 95% ethanol and diluted to 10 μM with Hank's balanced salt solution (HBSS) with 15 mM $MgCl_2$ and without phenol red (HBSS-15 mM $MgCl_2$; Gibco). The MIN6 cells were transfected with empty small interfering RNA (siRNA) (control) and Tmem30a siRNA (KD), respectively. After 72 h, transfected MIN6 cells were washed using PBS, equilibrated in pre-warmed HBSS-15 mM $MgCl_2$ for 15 min at 20°C, and incubated with 20 μM NBD-PS for 20 min at 20°C. Subsequently, the cells were washed with HBSS-15 mM $MgCl_2$ on ice. To quantify NBD-PS translocated into the inner leaflet of the plasma membrane, PS from the outer leaflet was removed by back-extraction. This was done by adding ice-cold HBSS supplemented with 2% bovine serum albumin (Sigma, St. Louis, MO, USA) to the cells for 10 min on ice and repeating the process three times. Finally, cells were centrifuged at 4°C for 5 min at 300 g and suspended in HBSS and analyzed with a flow cytometer (CytoFLEX, Beckman Coulter). The mean fluorescence intensity was calculated for each group. Dead cells were excluded from the analysis by blue fluorescence (DAPI positive). The NBD-PS fluorescence intensity of MIN6 cells was plotted on a histogram to calculate the MFI.

Statistical analysis

Statistical analysis was performed using GraphPad Prism 6 software. The datasets were tested for normal distribution using Shapiro-Wilk test. For normally distributed datasets, statistical significance was determined by Student's t test or ANOVA. If the dataset is not normally distributed, non-parametric statistic is used. p values were calculated by Student's t test or ANOVA followed by a Tukey, Dunnett, or Sidak's multiple comparisons test as appropriate. $p < 0.05$ was considered statistically significant.

SUPPLEMENTAL INFORMATION

Supplemental information can be found online at https://doi.org/10.1016/j.ymthe.2021.04.026.

ACKNOWLEDGMENTS

The authors would like to thank Chengdu LiLai Biotechnology Co., Ltd. for technical assistance with histology analysis and transmission electron microscopy service. This study was supported by grants from the Natural Science Foundation of China (81770950 and 81970841 to X.Z.), the National Key Research and Development Program of China (2017YFC0113901), and the Department of Science and Technology of Sichuan Province (2020JDZH0027, 2016TD0009, 2018JZ0019, 20ZYD038, and 20ZYD037). The funders had no role in the study design, data collection or analysis, decision to publish, or preparation of the manuscript. The authors alone are responsible for the content and writing of the paper.

AUTHOR CONTRIBUTIONS

X.Z. conceived the study. X.Z. and P.S. designed and supervised the study. Y.Y., W.L., and K.S. performed the animal analysis, cell biology, immunohistochemistry, and gene expression studies. W.T. and X.L. were responsible for animal breeding and genotyping. X.Z., Y.Y.,

and P.S. wrote the manuscript. All authors critically revised and gave final approval to this manuscript.

DECLARATION OF INTERESTS

The authors declare no competing interests.

REFERENCES

1. Kusminski, C.M., Shetty, S., Orci, L., Unger, R.H., and Scherer, P.E. (2009). Diabetes and apoptosis: lipotoxicity. Apoptosis *14*, 1484–1495.
2. Lindahl, M., Danilova, T., Palm, E., Lindholm, P., Võikar, V., Hakonen, E., Ustinov, J., Andressoo, J.O., Harvey, B.K., Otonkoski, T., et al. (2014). MANF is indispensable for the proliferation and survival of pancreatic β cells. Cell Rep. *7*, 366–375.
3. Morley, T.S., Xia, J.Y., and Scherer, P.E. (2015). Selective enhancement of insulin sensitivity in the mature adipocyte is sufficient for systemic metabolic improvements. Nat. Commun. *6*, 7906.
4. Liu, M., Wright, J., Guo, H., Xiong, Y., and Arvan, P. (2014). Proinsulin entry and transit through the endoplasmic reticulum in pancreatic beta cells. Vitam. Horm. *95*, 35–62.
5. Rorsman, P., and Renström, E. (2003). Insulin granule dynamics in pancreatic beta cells. Diabetologia *46*, 1029–1045.
6. MacDonald, P.E., Eliasson, L., and Rorsman, P. (2005). Calcium increases endocytotic vesicle size and accelerates membrane fission in insulin-secreting INS-1 cells. J. Cell Sci. *118*, 5911–5920.
7. Balasubramanian, K., and Schroit, A.J. (2003). Aminophospholipid asymmetry: A matter of life and death. Annu. Rev. Physiol. *65*, 701–734.
8. Graham, T.R. (2004). Flippases and vesicle-mediated protein transport. Trends Cell Biol. *14*, 670–677.
9. Panatala, R., Hennrich, H., and Holthuis, J.C.M. (2015). Inner workings and biological impact of phospholipid flippases. J. Cell Sci. *128*, 2021–2032.
10. Sebastian, T.T., Baldridge, R.D., Xu, P., and Graham, T.R. (2012). Phospholipid flippases: building asymmetric membranes and transport vesicles. Biochim. Biophys. Acta *1821*, 1068–1077.
11. Paulusma, C.C., Folmer, D.E., Ho-Mok, K.S., de Waart, D.R., Hilarius, P.M., Verhoeven, A.J., and Oude Elferink, R.P. (2008). ATP8B1 requires an accessory protein for endoplasmic reticulum exit and plasma membrane lipid flippase activity. Hepatology *47*, 268–278.
12. Saito, K., Fujimura-Kamada, K., Furuta, N., Kato, U., Umeda, M., and Tanaka, K. (2004). Cdc50p, a protein required for polarized growth, associates with the Drs2p P-type ATPase implicated in phospholipid translocation in Saccharomyces cerevisiae. Mol. Biol. Cell *15*, 3418–3432.
13. van der Velden, L.M., Wichers, C.G., van Breevoort, A.E., Coleman, J.A., Molday, R.S., Berger, R., Klomp, L.W., and van de Graaf, S.F. (2010). Heteromeric interactions required for abundance and subcellular localization of human CDC50 proteins and class 1 P4-ATPases. J. Biol. Chem. *285*, 40088–40096.
14. Folmer, D.E., Mok, K.S., de Wee, S.W., Duijst, S., Hiralall, J.K., Seppen, J., Oude Elferink, R.P., and Paulusma, C.C. (2012). Cellular localization and biochemical analysis of mammalian CDC50A, a glycosylated β-subunit for P4 ATPases. J. Histochem. Cytochem. *60*, 205–218.
15. Bryde, S., Hennrich, H., Verhulst, P.M., Devaux, P.F., Lenoir, G., and Holthuis, J.C. (2010). CDC50 proteins are critical components of the human class-1 P4-ATPase transport machinery. J. Biol. Chem. *285*, 40562–40572.
16. Takatsu, H., Baba, K., Shima, T., Umino, H., Kato, U., Umeda, M., Nakayama, K., and Shin, H.W. (2011). ATP9B, a P4-ATPase (a Putative Aminophospholipid Translocase), Localizes to the trans-Golgi Network in a CDC50 Protein-independent Manner. J. Biol. Chem. *286*, 38159–38167.
17. Yang, Y., Liu, W., Sun, K., Jiang, L., and Zhu, X. (2019). Tmem30a deficiency leads to retinal rod bipolar cell degeneration. J. Neurochem. *148*, 400–412.
18. Zhang, L., Yang, Y., Li, S., Zhang, S., Zhu, X., Tai, Z., Yang, M., Liu, Y., Guo, X., Chen, B., et al. (2017). Loss of Tmem30a leads to photoreceptor degeneration. Sci. Rep. *7*, 9296.
19. Liu, L., Zhang, L., Zhang, L., Yang, F., Zhu, X., Lu, Z., Yang, Y., Lu, H., Feng, L., Wang, Z., et al. (2017). Hepatic Tmem30a Deficiency Causes Intrahepatic Cholestasis by Impairing Expression and Localization of Bile Salt Transporters. Am. J. Pathol. *187*, 2775–2787.
20. Li, N., Yang, Y., Liang, C., Qiu, Q., Pan, C., Li, M., Yang, S., Chen, L., Zhu, X., and Hu, Y. (2018). Tmem30a Plays Critical Roles in Ensuring the Survival of Hematopoietic Cells and Leukemia Cells in Mice. Am. J. Pathol. *188*, 1457–1468.
21. Yang, Y., Sun, K., Liu, W., Zhang, L., Peng, K., Zhang, S., Li, S., Yang, M., Jiang, Z., Lu, F., and Zhu, X. (2018). Disruption of Tmem30a results in cerebellar ataxia and degeneration of Purkinje cells. Cell Death Dis. *9*, 899.
22. Zhang, S., Liu, W., Yang, Y., Sun, K., Li, S., Xu, H., Yang, M., Zhang, L., and Zhu, X. (2019). TMEM30A deficiency in endothelial cells impairs cell proliferation and angiogenesis. J. Cell Sci. *132*, jcs225052.
23. Dhar, M., Webb, L.S., Smith, L., Hauser, L., Johnson, D., and West, D.B. (2000). A novel ATPase on mouse chromosome 7 is a candidate gene for increased body fat. Physiol. Genomics *4*, 93–100.
24. Dhar, M.S., Sommardahl, C.S., Kirkland, T., Nelson, S., Donnell, R., Johnson, D.K., and Castellani, L.W. (2004). Mice heterozygous for Atp10c, a putative amphipath, represent a novel model of obesity and type 2 diabetes. J. Nutr. *134*, 799–805.
25. Dhar, M.S., Yuan, J.S., Elliott, S.B., and Sommardahl, C. (2006). A type IV P-type ATPase affects insulin-mediated glucose uptake in adipose tissue and skeletal muscle in mice. J. Nutr. Biochem. *17*, 811–820.
26. Surwit, R.S., Feinglos, M.N., Rodin, J., Sutherland, A., Petro, A.E., Opara, E.C., Kuhn, C.M., and Rebuffé-Scrive, M. (1995). Differential effects of fat and sucrose on the development of obesity and diabetes in C57BL/6J and A/J mice. Metabolism *44*, 645–651.
27. Ansari, I.U., Longacre, M.J., Paulusma, C.C., Stoker, S.W., Kendrick, M.A., and MacDonald, M.J. (2015). Characterization of P4 ATPase Phospholipid Translocases (Flippases) in Human and Rat Pancreatic Beta Cells: THEIR GENE SILENCING INHIBITS INSULIN SECRETION. J. Biol. Chem. *290*, 23110–23123.
28. Irvin, M.R., Wineinger, N.E., Rice, T.K., Pajewski, N.M., Kabagambe, E.K., Gu, C.C., Pankow, J., North, K.E., Wilk, J.B., Freedman, B.I., et al. (2011). Genome-wide detection of allele specific copy number variation associated with insulin resistance in African Americans from the HyperGEN study. PLoS ONE *6*, e24052.
29. Milagro, F.I., Campión, J., Cordero, P., Goyenechea, E., Gómez-Uriz, A.M., Abete, I., Zulet, M.A., and Martínez, J.A. (2011). A dual epigenomic approach for the search of obesity biomarkers: DNA methylation in relation to diet-induced weight loss. FASEB J. *25*, 1378–1389.
30. Postic, C., Shiota, M., Niswender, K.D., Jetton, T.L., Chen, Y., Moates, J.M., Shelton, K.D., Lindner, J., Cherrington, A.D., and Magnuson, M.A. (1999). Dual roles for glucokinase in glucose homeostasis as determined by liver and pancreatic beta cell-specific gene knock-outs using Cre recombinase. J. Biol. Chem. *274*, 305–315.
31. Pechhold, K., Zhu, X., Harrison, V.S., Lee, J., Chakrabarty, S., Koczwara, K., Gavrilova, O., and Harlan, D.M. (2009). Dynamic changes in pancreatic endocrine cell abundance, distribution, and function in antigen-induced and spontaneous autoimmune diabetes. Diabetes *58*, 1175–1184.
32. Cohen, J.C., Horton, J.D., and Hobbs, H.H. (2011). Human fatty liver disease: old questions and new insights. Science *332*, 1519–1523.
33. Gurevich-Panigrahi, T., Panigrahi, S., Wiechec, E., and Los, M. (2009). Obesity: pathophysiology and clinical management. Curr. Med. Chem. *16*, 506–521.
34. Rinella, M.E. (2015). Nonalcoholic fatty liver disease: a systematic review. JAMA *313*, 2263–2273.
35. Tong, Q., Ye, C.P., Jones, J.E., Elmquist, J.K., and Lowell, B.B. (2008). Synaptic release of GABA by AgRP neurons is required for normal regulation of energy balance. Nat. Neurosci. *11*, 998–1000.
36. Gall, W.E., Geething, N.C., Hua, Z., Ingram, M.F., Liu, K., Chen, S.I., and Graham, T.R. (2002). Drs2p-dependent formation of exocytic clathrin-coated vesicles in vivo. Curr. Biol. *12*, 1623–1627.
37. Thorens, B., Gérard, N., and Dériaz, N. (1993). GLUT2 surface expression and intracellular transport via the constitutive pathway in pancreatic beta cells and insulinoma: evidence for a block in trans-Golgi network exit by brefeldin A. J. Cell Biol. *123*, 1687–1694.

38. Chakrabarti, S.K., James, J.C., and Mirmira, R.G. (2002). Quantitative assessment of gene targeting in vitro and in vivo by the pancreatic transcription factor, Pdx1. Importance of chromatin structure in directing promoter binding. J. Biol. Chem. *277*, 13286–13293.

39. Kline, C.F., Wright, P.J., Koval, O.M., Zmuda, E.J., Johnson, B.L., Anderson, M.E., Hai, T., Hund, T.J., and Mohler, P.J. (2013). βIV-Spectrin and CaMKII facilitate Kir6.2 regulation in pancreatic beta cells. Proc. Natl. Acad. Sci. USA *110*, 17576–17581.

40. Barg, S., Ma, X., Eliasson, L., Galvanovskis, J., Göpel, S.O., Obermüller, S., Platzer, J., Renström, E., Trus, M., Atlas, D., et al. (2001). Fast exocytosis with few Ca(2+) channels in insulin-secreting mouse pancreatic B cells. Biophys. J. *81*, 3308–3323.

41. Folmer, D.E., Elferink, R.P., and Paulusma, C.C. (2009). P4 ATPases - lipid flippases and their role in disease. Biochim. Biophys. Acta *1791*, 628–635.

42. Pomorski, T., Lombardi, R., Riezman, H., Devaux, P.F., van Meer, G., and Holthuis, J.C. (2003). Drs2p-related P-type ATPases Dnf1p and Dnf2p are required for phospholipid translocation across the yeast plasma membrane and serve a role in endocytosis. Mol. Biol. Cell *14*, 1240–1254.

43. Spiegelman B., M., and Flier J., S. (2001). Obesity and the regulation of energy balance. Cell *104*, 531–543.

44. Boden, G. (1997). Role of fatty acids in the pathogenesis of insulin resistance and NIDDM. Diabetes *46*, 3–10.

45. McGarry, J.D. (2002). Banting lecture 2001: Dysregulation of fatty acid metabolism in the etiology of type2diabetes. Diabetes *51*, 7–18.

46. Austin, B.P., Garthwaite, T.L., Hagen, T.C., Stevens, J.O., and Menahan, L.A. (1984). Hormonal, metabolic and morphologic studies of aged C57BL/6J obese mice. Exp. Gerontol. *19*, 121–132.

47. Zhao, L., Rosales, C., Seburn, K., Ron, D., and Ackerman, S.L. (2010). Alteration of the unfolded protein response modifies neurodegeneration in a mouse model of Marinesco-Sjögren syndrome. Hum. Mol. Genet. *19*, 25–35.

48. Zhu, X., Libby, R.T., de Vries, W.N., Smith, R.S., Wright, D.L., Bronson, R.T., Seburn, K.L., and John, S.W. (2012). Mutations in a P-type ATPase gene cause axonal degeneration. PLoS Genet. *8*, e1002853.